THE THREE-DIMENSIONAL STRUCTURE OF THE SUMMIT MAGMA COMPLEX AT KILAUEA VOLCANO, HAWAII, FROM TRAVEL TIME CDI TOMOGRAPHY

By

Aaron David Pearson

RECOMMENDED:

Roger A. Hansen

Douglas H Christensen
Advisory Committee Chair

Department Head

APPROVED:

Dean, College of Science, Engineering and Mathematics

Dean of the Graduate School

3-12-01
Date

THE THREE-DIMENSIONAL STRUCTURE OF THE SUMMIT MAGMA COMPLEX AT KILAUEA VOLCANO, HAWAII, FROM TRAVEL TIME CDI TOMOGRAPHY

A

THESIS

Presented to the Faculty

of the University of Alaska Fairbanks

in Partial Fulfillment of the Requirements

for the Degree of

MASTER OF SCIENCE

By

Aaron David Pearson, B.S.

Fairbanks, Alaska

May 2001

Abstract

Methods of seismic tomography have been applied to Kilauea Volcano, Hawaii several times to determine the structure of the magma conduit system. The shallow summit chambers are the least defined part of the magma system. A dense seismic array (~100 stations over ~10x10 km^2) was deployed over the summit in January, 1996 and February, 1997. P- and S- phase travel times of 271 earthquakes recorded at these stations were inverted with a new tomography algorithm developed by Clippard (1998) to highlight small, anomalous regions. A large (26.2 km^3) low P-phase velocity anomaly (9% perturbation) was imaged beneath the summit caldera impling a body of approximately 9% partial melt. Several small anomalies of Vp/Vs = 2.7 beneath Kilauea caldera and the East Rift Zone are also interpreted as localized pockets of melt, gas and/or highly fractured material.

LIST OF FIGURES

LIST OF TABLES

Acknowledgements

This project would not have been possible without the support of my advisory committee: Doug Christensen, Steve McNutt, and Roger Hansen. Several other Geophysical Institute fixtures were repeatedly called on for assistance in matters technical and otherwise, most notably Kent Lindquist, Mitch Robinson, Dan McNamara, Scott Stihler, and Rowdy LaFevers. Much lavish parise should also be heaped upon the grad student community, for intellectual support and endless distraction. Decorum prevents me from listing any details here, but suffice it to say that the third floor seimology lab would be a fitting site for a soap opera or pulp fiction novel. The denizens of the galciology lab provided relief from the tidiness and order of the third floor, and Miss Karoline Frey was a welcome break from them. Finally, special the National Science Foundation should be thanked (grant number ******) for their generous financial support.

Introduction

Geologic History and Structure

Kilauea Volcano is a broad, low relief shield volcano. It covers 1500 km^2 and has a summit elevation of 1240 m. There are seven prominent structural zones: two rift zones, three fault zones, Halemaumau crater, and the Kilauea caldera (Figure 1) (Hill and Zucca, 1987). The Southwest Rift Zone (SWRZ) extends to the southwest of Halemaumau crater, and the East Rift Zone (ERZ) extends to the east. The rift zones are marked by craters, cinder cones, and fissures. The rift zones and Halemaumau crater are the source of virtually all eruptions. The boundary formed by these three structures separates Kilauea into a north flank, buttressed by the adjacent Mauna Loa Volcano, and a mobile south flank.

There have been 58 eruptions from 1823, when written records began, through 1999 (Macdonald et al., 1986; Hawaiian Volcano Observatory, 1999). They have ranged in duration from less than one day to 17 years, though most are on the order of a few weeks. The average basaltic lava volume for an eruption is 0.054 km^3. Volumes range from 0.000022 km^3 to 1.6 km^3 in the current ongoing eruption. There have also been several explosive eruptions without lava flow. The current eruption began on January 3, 1983, with eruptive episodes broken into 54 phases to date. Recent activity has been concentrated at Pu'u 'O'o and Kupaianaha craters in the ERZ (Hawaiian Volcano Observatory, 1999). Given the short time period of this study, it is important to note that the 17-year ongoing eruption indicates a stable magma plumbing system.

There are three main fault zones near Kilauea (Figure 1). Throughout the volcano, faulting is generally normal and strikes east-northeast. The Koae fault zone intersects and connects the ERZ and the SWRZ. The Hilina fault zone is sub-parallel to the south coast. It is controlled by the seaward slumping of the south flank (Rowan and Clayton, 1993). The Kaoiki fault zone actually lies on the south flank of Mauna Loa, to the north of and parallel to the SWRZ. It is included here because it is the most seismically active fault zone on the island of Hawaii.

A significant part of the magma plumbing system beneath Kilauea is well defined, from the mantle conduit to the rift zones. This is a result of 40 years of work with seimologic and deformation observations since the basic plumbing system for a Hawaiian volcano was first outlined by Eaton and Murata (1960).

Kilauea's mantle conduit can be defined by earthquake hypocenters. Although there is no direct correlation between clusters of seismicity and the presence of magma, some assumptions can be made: swarm seismicity takes place in regions of dike intrusion or magma conduits; and an aseismic zone adjacent to an area of volcanic seismicity can be interpreted as a magma storage zone (S. McNutt, pers. com.). Based on this reasoning, the conduit is interpreted to rise from the upper mantle (~60 km), through the oceanic crust (14 km), and into the base of the volcanic edifice (6.5 km) (all depths are relative to, and positive below, mean sea level) (Ryan et al., 1981). The diameter of the conduit is about 3 km, centered below Halemaumau crater and the summit reservoir. Deeper than 20 km, the diameter of the conduit system widens to

around 13 km (Klein et al., 1987). Above 6 km depth, the magma conduit system is less well defined.

Long-period events are characterized by emergent P-waves and dominant frequencies of 1-5 Hz. Volcanic tremor has the same frequency range, but has no distinct onset and a duration of minutes to days or longer (McNutt, 1996). These two types of events are inferred to have the same source: fluid-pressurization processes; shear failure; tensile failure; or non-linear flow processes. At Kilauea, tremor has been associated with magma movement and eruptive activity (Koyanagi et al., 1987) There are three depth zones defined by long-period hypocenters and inferred tremor source: The first is from 0-5 km beneath the summit and rift zones and is associated with summit deflation and eruption. The second extends from 5-15 km beneath Kilauea and is associated with summit inflation. The deepest zone is from 30-60 km. The gap between 15 and 30 km is interpreted to be a low stress region that allows steady flow of magma (Koyanagi et al., 1987).

Previous Geophysical Research

The history of seismic monitoring in Hawaii begins in 1912 with the formation of the Hawaiian Volcano Observatory (HVO) (Klein and Koyanagi, 1980). A solar-corrected clock for event timing, a smoked paper drum recorder, and a pendulum used for the detection of east-west motion was some of the equipment at the observatory in its first year. By December 1955, there were 8 time synchronized stations on the Island of Hawaii, with 18 components. In 1975, a tape recorder was installed, and three years later a computer and digitizer were added to allow playback (Klein and Koyanagi,

1980). Today there are over 60 stations on the Island of Hawaii, most have three-component short-period sensors, and some are broadband.

Methods of seismic tomography have been successfully applied to Kilauea several times, at different scales and using both teleseisms and local earthquakes as sources (Table 1) (Ellsworth and Koyanagi, 1977; Thurber, 1984; Rowan and Clayton, 1993; Okubo et al., 1997; Dawson et al., 1999). Each of these studies imaged high-Vp anomalies, from ~1.5 to 2 km/s higher than background, beneath the summit caldera. Workers interpreted them to be dense intrusives that form the containment boundaries for the partial melt at the summit, centered ~2 km south of Halemaumau crater at a depth of 0-3 km, and beneath the ridges of the rift zones. The presence of this partial melt body is further supported by the observation of changes in the surface elevation (Jaggar and Finch, 1929; Swanson et al., 1979; Fiske and Kinoshita, 1969). A core of dense intrusive rock surrounding the conduit system and magma chamber has been interpreted to be the cause of high Bouger gravity anomalies at the summit of Kilauea (Hill and Zucca, 1987).

Low P-phase velocity anomalies, ~0.5 km/s less than background, have been imaged at the summit in two studies. The single anomaly imaged in Thurber (1984) coincides precisely with an aseismic zone and was interpreted to be the summit magma complex. The roughly spherical region is 3 km in diameter and centered at 1 km depth beneath Halemaumau crater. Dawson et al. (1999) attributed the shallow anomalies (-1 to 0 km depth) imaged in their study to be a fracture system, ash and tephra deposits,

Table 1: Tomography studies at Kilauea.

study	technique*	coverage	grid size/node spacing	study volume
Ellsworth and Koyanagi (1977)	damped least-squares (Aki et al., 1977)	164 teleseismic events, recorded at 26 stations. 2112 P-wave arrivals.	x-y: 7.5 km, z: 12.5 km (1st layer), 15 km	x-y: 67.5x67.5 km, z: 72.5 km
Thurber (1984)	parameter separation and approximate ray tracing (ART) / damped least-squares.	85 local earthquakes, recorded at 17 stations.	x: 4 km, y-z: 3 km	x: 30 km, y: 20 km, z: 10 km
Rowan and Clayton (1993)	iterative back projection / damped least-squares.	12,295 local earthquakes, recorded at 42 stations. 111,600 P-wave arrivals.	2 grid sizes: 1x1x1 km and 5x5x5 km	2 regions: x: 100, 60 km, y: 55, 30 km, z: 50, 50 km
Okubo et al. (1997)	finite difference ray tracing (Benz et al.,1996) / damped least-squares.	4,754 local earthquakes, recorded at 42 stations	x-y: 1 km, z: 2 km	x: ~95 km, y: ~55 km, z: 11 km
Dawson et al. (1999)	finite difference ray tracing (Benz et al.,1996) / damped least-squares. Vp/Vs structure also determined. *	206 local earthquakes, recorded at 67 stations. 4695 P- and 3195 S-wave arrivals	0.5x0.5x0.5 km	Vp: 15x15x15 km Vp/Vs: x-y: 10x10 km, z: 5km

* Vp/Vs inversion was done only in Dawson et al. (1999)

and shallow hydrothermal effects. A larger anomalous volume, from 0 to 4 km depth below the summit, is attributed to the presence of partial melt.

Summit Magma Chamber

The results of Dawson et al.'s (1999) recent work are particularly relevant to this study, since both used similar data sets and the region imaged in Dawson et al. (1999) is comparable to the 16.25 x 16.25 x 6 km region in the current study. As in the other

tomography studies at Kilauea, they found high P-wave anomalies beneath the SWRZ, the ERZ, and the along the edge of the summit caldera at shallow depths. A distinct (up to 10% contrast from the starting model) low P-phase velocity anomaly was found, centered beneath the SSE edge of the caldera and extending from 1 to 4 km below the surface. They also imaged the Vp/Vs ratio, and found a high ratio in the same region as the low P-phase anomaly. It is separated into two distinct lobes, one beneath the upper ERZ and the other beneath the southern portion of the caldera. They interpreted this to be highly fractured material, partial melt, or both.

However, there is still debate about the actual size and shape of the summit magma reservoir. Lower volume estimates consider only the active portion of the chamber. An examination of arc and hotspot volcanoes has shown a correlation between vent size and the lateral extent of source chambers. The implies that the active portion of the chamber is a tabular body, commonly 10% of the total chamber volume (S. McNutt, pers. com., Smith, 1960). At Kilauea, active chamber volume estimates range from ~0.08 km^3, the product of the volcano's average eruption rate and repose period (Klein, 1982); to ~2-3 km^3, based on a recent analysis of the residence time of geochemical fluctuations (Pietruszka and Garcia, 1999); and ~2-13 km^3, from the modeling of post-eruptive subsidence from geodetic and gravity data (Johnson, 1992).

A higher volume estimate is ~40 km^3, from the volume of the aseismic zone (Klein et al., 1987). Dawson et al. (1999) assume that the presence of partial melt and/or zoned magma storage regions contribute to the anomalously low P-phase velocities. They calculate an anomaly volume of 27 km^3, from the number of cells with

a P-phase velocity less than or equal to 95% of the starting model velocity. It should be noted that volume estimation is complicated by the likely presence of a zoned body: a hotter molten core surrounded by a partially crystallized zone and a hot ductile region (Pietruszka and Garcia, 1999). In a P-phase velocity inversion, such a region would be imaged as a highVp anomaly.

Deformation studies are also an important method of determining the location of a magma body, and are especially helpful when used in conjunction with seismic investigations. Using the point-source model introduced by Mogi (1958), it is possible to determine the center of deformation in an inflation event. The model assumes that the earth's crust is an elastic half-space, and that deformation is caused by a spherical pressure source whose radius is small compared with depth. The change in vertical deformation with horizontal distance from the source is sensitive to source depth. Leveling data can be plotted against a family of depth curves based on the point-source model, and the curve that best fits the data indicates source depth. The motion of magma through the conduit system can thus be tracked as the center of deformation shifts (e.g., Fiske and Kinoshita, 1969).

There are two opposing interpretations of the shape of the summit magma reservoir. Fiske and Kinoshita (1969) originally interpreted the reservoir to be a plexus of dikes and sills, centered at a depth of ~2 km beneath a point ~2 km to the southeast of Halemaumau crater. The center of inflation of the summit migrates over time, and the rate of vertical deformation changes during the course of an inflation event. Further, as the volcano grew to its present size, the reservoir migrated upward, leaving layers of

dense sills and feeder dikes behind at deeper levels. This interpretation is further supported by geology. The interior of Kilauea is made up of outwardly dipping lava flows, providing lateral zones of weakness for the formation of sills. Also, outcrops at Koolau volcano on Ohau expose extensive dike complexes in association with the main fissure complex (Takasaki et al., 1969).

However, recent analysis of leveling and trilateration data supports a model with a single, simple, reservoir source at the summit, accompanied by the outward growth of dikes during inflation. The source is centered at a depth of 1.6 km beneath a point ~2 km to the southeast of Halemaumau crater (Yang et al., 1992). Pietruszka and Garcia (1999) found that systematic changes in lava chemistry over time also suggest a relatively simple summit reservoir.

This Study

The goal of this work is to obtain a detailed, three-dimensional image of Kilauea's summit magma reservoir in order to better understand the volcano's entire magma supply system. Towards this end, a dense seismic array (average station spacing is ~1 km) was deployed around the summit of Kilauea Volcano by a group of international researchers under the Japan-United States Science and Technology (JUST) agreement. Travel times of earthquakes recorded at these stations were inverted with a new tomography algorithm designed to highlight small, anomalous regions. Unlike a traditional least-squares inversion which tends to attenuate and blur images, the algorithm, discussed in detail in a later section, tends to minimize the size of anomalous regions and allows high amplitude anomalies to be resolved (Clippard, 1998, Clippard

et al., 1995). The resulting images help answer questions about the size and shape of the summit magma reservoir system.

Data

In January 1996 and February 1997, a group of international researchers deployed up to 214 portable seismographs in dense arrays around the summit of Kilauea Volcano (Figures 2,3,4), under the JUST agreement (McNutt et al., 1997). This effort resulted in the most detailed seismic recording ever to take place on Kilauea, and the densest network to be assembled on a volcano. Approximately 12,000 P- and S-phase arrivals were picked from the data recorded during these two periods (01-11-96 through 02-01-96 and 02-06-97 through 02-12-97), from local earthquakes distributed beneath the array. The data from the two periods were analyzed together; it is assumed that structures imaged are temporally persistent.

Eruptive Activity During the Study Periods

Kilauea's ERZ has been in a continuous state of eruption since January 1983, with activity at Pu'u 'O'o, Kupaianaha, and Napau craters (Figure 1) (Heliker et al., 1998). The eruption has been broken into a series of episodes; currently episode 55 is ongoing (Hawaiian Volcano Observatory, 1999). During the eruption, there have been numerous swarms of microearthquakes associated with dike intrusion beneath the summit caldera and the ERZ (Okubo et al., 1996). A brief description of the seismicity and associated volcanism that occurred during the two JUST recording experiments follows.

Episode 53 began on February 20, 1993 with the opening of a new vent in Pu'u 'O'o crater. The episode ended on January 29, 1997, when flows abated (Heliker et al., 1998). A strong earthquake swarm occurred on February 1, 1996, during episode 53

and the 1996 JUST experiment (Okubo et al., 1996; McNutt et al., 1997). The swarm began at 0800 h HST, and was immediately followed by the onset of volcanic tremor and inflation at the summit. Tilt reached its maximum value at 1200 h. This was followed by long-period earthquakes beneath the summit caldera and summit deflation. The seismicity patterns resembled those associated with other occurrences of summit and upper ERZ intrusion (Okubo et al., 1996).

Eruptive episode 54 began on January 30, 1997, shortly after the end of episode 53, with the opening of a new vent on the floor of Napau crater (Figure 1). The episode continued for 24 hours (Thornber et al., 1997). Kilauea remained eruptively quiet for the entirety of the 1997 JUST experiment, until episode 55 began on February 24, 1997 (Hawaiian Volcano Observatory, 1999). However, moderate levels of microseismicity (several locatable events per day) were recorded throughout the 1997 experiment.

1996 Experiment

During the 1996 experiment, three dense arrays of seismographs were deployed and operated synchronously (Figures 2, 3) (McNutt et al., 1997). The arrays were designed to optimally record events under the summit caldera of Kilauea. The "A-antenna" was a 300 m aperture array, which consisted of 31 three-component seismographs arranged in three semi-circular arcs around a central receiver (Figure 3). The "C-array" consisted of two concentric rings surrounding a central station, C00 (Figure 2). Their diameters were 3 and 6 km, and they contained 8 and 16 three-component seismographs, respectively. Additional stations were added to the SW and NW arms of the array. There were a total of 40 stations in the "C-array". The "B-line"

array consisted of 43 vertical and 5 three-component seismographs spaced 35 m apart in a 1.7 km line oriented SSE from station C00. GPS-determined station location precision was on the order of a few centimeters.

1997 Experiment

During the 1997 experiment, two small aperture antennas (51 and 22 stations) and a 12 station rectangular net (~1 km x 0.75 km) were deployed near the summit caldera (Figure 4). Fifteen stations, including three clusters with ~0.5 km spacing were also deployed over the summit area. Five of these stations were equipped with both broadband and short period sensors (Figure 4).

Instrumentation

All sensors during both experiments were Mark Products L-22D short period seismometers, except for the five broadband sensors in the 1997 experiment. The L-22D instruments have a natural period of 2 Hz (+/- 10%), and 0.707 critical damping. The broadband sensors were Streckheisen STS 2's that have corner frequencies of 0.0083 Hz (120 s) and 50 Hz. Small, portable, digital data loggers manufactured by Hakusan Corporation, Tokyo, recorded up to three seismic data channels and a GPS time signal. Data were recorded at 100 samples per second. In 1996, the data loggers were run in continuous mode for 9-hour collection periods during the night from January 11 through January 21, and in event- triggered mode until the end of the experiment, except during the swarm of February 1, when continuous mode was used again. In 1997, recording was continuous from February 6 through February 11, with the exception of a few outages of several hours duration. At the end of each daily

recording session, the data were uploaded from the data loggers onto laptop computers, then written to HVO workstations. Over 40 GB of data were collected during the experiment (McNutt et al., 1997) and archived in a CSS Datascope database (Quinlan, 1998).

Data Conversion

The continuous data were parsed into 15 minute segments in order to apply time corrections. During the 1996 recording period, the continuous data were locked to GPS time at the beginning and end of each 9-hour recording session. Over the course of a day, the data logger's clock would drift by as much as 0.1 seconds. It was important that the data be corrected back to GPS time as accurately as possible in order to take advantage of the sample interval, 0.01 s. In 1997, an improved procedure was used in which the data were locked to GPS time every hour, and thus did not require time corrections. It was noted that the time shifts at each hour from the 1997 data were approximately the same over the recording period (Figure 5). For the 1996 data, therefore, it seemed reasonable to divide the total time shift over the session by 36 (the number of 15 minute segments), then shift each segment by that amount.

Phase Travel Time Selection

Phase data from the 1996 and 1997 JUST experiments were used in this study. In addition, data were supplemented by the HVO's phase picks at HVO stations during the same time period. The total number of stations used is 249. Earthquakes were identified and P- and S-phases were picked manually using Datscope's dbpick software. P-phases were picked for every event with an impulsive onset, and S-phases were found

at many stations, especially those with horizontal components. The precision of the picks is 0.01 s, limited by the sample rate (100/s). P-phase pick error is typically less than 0.05 s, and S-phase error is typically less than 0.1 s. The arrival times were sorted chronologically and grouped into separate events. To be used in an inversion, the arrivals had to pass a set of criteria. Arrivals were not used if the event had an azimuthal gap greater than or equal to 210°. After the first inversion (discussed below), each arrival was weighted by proportional error. Proportional error is travel time residual divided by total travel time (Figure 6). Full weight is given to arrivals with a proportional error less than 0.075, zero weight is given to those with errors greater than 0.25. An event must have at least 7 arrivals to be included, 4 of which must be P-phases. A total of 271 of the original 551 events passed these criteria, with 8246 P- and S-phase arrivals.

Algorithms

The location, ray-tracing, and tomography algorithms are all parts of a software package developed by James D. Clippard as part of a University of Alaska Fairbanks PhD thesis (Clippard, 1998). The tomography algorithm requires five inputs: earthquake arrival times, station locations, topography, a starting velocity model, and a set of constraints for the inversion. First, a summary of the theory behind Composite Distribution Inversion (CDI) and ray tracing algorithms will be given, then the procedure used in this study will be discussed.

CDI

CDI was developed specifically to image discrete features in a known background (Clippard et al., 1995; Clippard, 1998). The method assumes that model parameters (e.g., a set of seismic velocities) are members of one of two subpopulations, both with Gaussian distributions: either a low-variance population for background parameters or a high-variance population for anomalous parameters. Both populations have 0 covariance. In a high variance population, the effect of error reduction has a far greater effect on parameter estimation than path length reduction. This allows the amplitude of the anomalous values to be less attenuated as the entire model is inverted.

CDI is implemented through an iterative weighting scheme within a standard least-squares inversion. Since there is usually no a priori information as to which parameters belong in which population, an iterative probabilistic approach is used for population assignment during inversion. CDI thus allows high-amplitude anomalies in truly anomalous regions, while still stabilizing the background.

This approach is markedly different from the traditional damped least-squares method. A least-squares inversion minimizes prediction error and solution length simultaneously for the entire set of model parameters. The result is that anomalous values are attenuated and distributed (smeared) over a larger region. In a study volume containing discrete anomalies, the final least-squares image is highly smoothed and the anomalies are poorly resolved (Clippard, 1998).

CDI was used to image a 2 m diameter tunnel within the1520 m^2 region between souce and receiver boreholes (Clippard, 1998, Clippard et al., 1995). Air in the tunnel was imaged as a low-Vp anomaly (13% perturbation) within a ~4.85 km/s background. CDI has also been used to image low-Vp anomalies of up to 12% background at three Alaskan volcanoes: Redoubt, Spurr, and Augustine (Clippard, 1998).

Ray Tracing

Accurate ray tracing is an important element of tomographic inversion. In this study a computationally efficient general method is used, as developed by Clippard (1998). This hybrid method first uses graph theory (Klimes and Kvasnicka, 1994) to provide approximate raypaths and then a variation of pseudo-bending (Um and Thurber, 1987) for ray refinement.

Graph theoretic ray tracing (Klimes and Kvasnicka, 1994) finds the minimum travel time path from a set of possible connections between nodes in the grid. Raypath segments are allowed between any node in the network and a finite number of nearby nodes. A set of nodes of known slowness is required at the start, and the travel time field expands across the network. Though graph theory based travel time field

computation is robust and efficient with coarse node spacing, computational experiments indicate that a rapidly increasing amount of computer memory and CPU time are required with finer node spacing to remove the last few percent of error.

Further refinement of the ray path is done with pseudo-bending (Um and Thurber, 1987), which operates sequentially on each set of three nodes of an initial raypath. The end nodes of each set are held fixed, and the center node is perturbed along a path defined by the ray's curvature. After the entire ray has been sequentially perturbed, error is checked against a pre-set "improvement" constraint. If error is greater than the constraint, a new node is added between each existing node, and the three node sequential perturbation is repeated. The pseudo-bending algorithm also allows the topography to be used as a boundary, so that rays will not be traced above the surface. (Clippard, 1998; Um and Thurber, 1987).

Procedure

CDI tomography requires a well constrained starting model from which anomalous features are imaged. Three inversions were required to produce the final CDI model, each successive inversion over a finer grid spacing and smaller volume. The first two inversions were damped least squares, and they served to generate a well constrained starting model for CDI. Two model parameters were inverted in each case, Vp and Vs/Vp ratio. This allows for simple computation of Vs and Vp/Vs models after inversion, while Vp and Vs arrival data remain coupled during the inversion. The parameters displayed and discussed are Vp and Vp/Vs. The least-squares algorithm used for each inversion was the iterative LSQR (Paige and Saunders, 1982)

Initial 1D Model

The first step was to determine a 1D Vp and Vs gradient model for input into the first inversion. This was accomplished by subjectively examining the output of several trial inversions using a variety of input initial models. All trial inversions revealed a Vp of ~4 km/s in the upper layers, regardless of the input model. The root-mean-square (RMS) of P-phase travel time residuals after inversion varied little with the initial Vp model, but was very sensitive to changes in the Vs model.

Clippard (1998) developed a method of determining a Vp/Vs ratio for the initial model that does not require hypocenters. There are two assumptions: that P- and S-phases follow the same raypath, and that the Vp/Vs ratio is constant throughout the model. Given a single source a, two stations b and c, and the respective arrival times

T_{ab} and T_{ac}, the ratio of observed S- and P-phase arrival time differences can be used to calculate the Vp/Vs ratio as shown below:

$$\frac{T_{ab}^{s} - T_{ac}^{s}}{T_{ab}^{p} - T_{ac}^{p}} = k = \frac{Vp}{Vs}$$

Details of this derivation can be found in Clippard (1998). This calculation was performed for each pair of arrivals (9897 pairs), resulting in a median Vp/Vs ratio of 1.77 (Figure 7). This value was used to compute the initial Vs model.

A layer is added at the bottom (25 km) of all initial models with a faster velocity than the one above to insure a non-zero velocity gradient, as a gradient is required for the pseudo-bending algorithm (Um and Thurber, 1987). The initial 1D model is listed in Table 2. Below the shallow layers, this 1D model is similar to HG50 (Table 3), the gradient model currently used by HVO for locations (Klein, 1981).

Table 2: Initial 1D gradient model. Depth is to top of layer. Vp/Vs = 1.77

depth (km)	Vp (km/s)
-2.5	3.5
0	4
2.5	5
7.5	7
25	8.4

Table 3: HG50 gradient model. Depth is to top of layer. (Klein, 1981)

depth (km)	Vp (km/s)
0	1.9
4.6	6.5
15	6.9
16.5	8.3

Large-scale Damped Least-Squares

A large volume was used for the first 3D inversion, 68 x 68 km to a depth of 24 km. It is horizontally centered at a point on the southwest rim of Kilauea caldera (19.392° N, 155.287° W) (Figure 1), approximately in the middle of the JUST recording network. The cells were 2 x 2 x 2 km. The overdamped (smoothing constraint = 0.8) inversion over large grid spacing revealed little structure.

The main purpose of this large-scale inversion was to provide locations using earthquakes and stations outside the final small CDI study volume. Although some of these raypaths did not travel through the volume used for CDI, those that did increased the range of ray azimuths for each cell they crossed. Earthquakes were relocated after each of three iterations in the inversion. Three iterations were used in the large- and medium-scale inversions, as this effectively reduced residuals and was computationally efficient. In both cases, further iterations reduced residuals by less than a percent.

Medium-Scale Damped Least-Squares

The medium-scale inversion was performed on a smaller volume 31 x 31 km to 8 km depth with the same center (Figure 1), using the output of the large-scale inversion

as the starting model. Cells were 1 x 1 x 1 km. Raypaths that propagated partly outside of the inverse volume did so through cells that retained their parameters from the large-scale model. Inversions were completed with five different smoothing constraints: 0.05, 0.1, 0.2, 0.4, and 0.8. The model with a smoothing of 0.4 was chosen as the one that was most related to actual geologic structure, based on residual reduction and subjective criteria. Selected depth sections of the Vp and Vp/Vs models from this inversion are shown in Figures 8a-h. The model created with a smoothing constraint of 0.8 was then used as the starting model for CDI. The model from this overdamped inversion was considered the best estimate of a smooth background model for input into CDI. Relocations after the final iteration of the overly smoothed inversion showed a reduction in P-phase residual RMS of 80%, from 0.871 to 0.171 s.

Fine-Scale CDI

The final CDI run was performed on a volume 16.25 x 16.25 km (Figure 1) and extending to a depth of 5.25 km. Vp and Vs/Vp were computed in 0.25 x 0.25 x 0.25 km cells.

There are several a priori CDI settings that constrain the inversion. First is the proportion of the number of cells whose parameters fall into the background versus the anomaly populations. This proportion weights the low variance (background) versus high variance (anomaly) probability functions. Then within each population a standard deviation is set for both Vp and Vs/Vp. Inversions were computed for 33 different constraint combinations (Table 4), yielding images whose anomalies varied slightly in spatial extent and amplitude but showed the same basic structures. The constraints used

Table 4: CDI constraint combinations tried. Constraints used for the final model (Figures 12, 14, 16, and 18) in bold type.

background %	anomaly %	background Vp std. dev.	background Vs/Vp std. dev.	Anomaly Vp std.dev.	anomaly Vs/Vp std.dev
5	95	2	0.5	5	1
30	70	20	5	45	9
30	70	80	20	120	24
35	65	2	0.5	5	1
50	50	0.5	0.125	1.25	0.25
50	50	1.5	0.375	3.75	0.75
50	50	10	2.5	55	11
50	50	10	2.5	80	16
50	50	10	2.5	25	5
50	50	12	3	40	8
50	50	15	3.75	20	4
50	50	15	3.75	25	5
50	50	2	0.5	5	1
50	50	2.5	0.625	6.25	1.25
50	50	20	5	120	24
50	50	20	5	45	9
50	50	20	5	65	13
50	50	20	4	10	2
50	50	20	4	100	20
50	50	40	10	100	20
50	50	40	10	65	13
50	50	40	10	80	16
50	50	5	1.25	8	1.6
50	50	5	1.25	12	2.4
50	50	50	12.5	120	24
50	50	60	15	100	20
50	50	80	20	120	24
65	35	2	0.5	5	1
70	30	20	5	45	9
70	30	80	20	120	24
80	**20**	**8**	**4**	**100**	**20**
80	20	10	2.5	25	5
95	5	10	2	10	2

in the final CDI run were those that best reduced travel time residual RMS and produced a coherent model.

The standard deviations in the final set of constraints are far higher than those that would describe an actual Vp or Vs/Vp data set. It is important to note that these are only boundaries for the purpose of constraining the inversion- the anomaly standard deviation settings imply that the parameter values are nearly unconstrained. The equivalent damping parameters for background Vp, background Vs/Vp, anomaly Vp, and anomaly Vs/Vp are 0.125, 0.25, 0.01, and 0.05, respectively. Anomalous population parameters are determined almost entirely by minimizing prediction error, while the solution of background parameters minimizes prediction error and solution length more equally.

After the 25th and final CDI iteration, event relocation showed that the RMS of the P-phase travel time residuals was reduced by 88.38% from relocation after the large-scale inversion, or 59% from the medium-scale inversion, to 0.101 s. The S-phase residual RMS was reduced by 37% overall from 0.217 to 0.137 s. The 25th iteration reduced P-phase residual RMS by 88.38% versus 88.33% after the 6th iteration. Though the inversion did not formally converge, the decrease in residual RMS from one iteration to the next became negligible.

Results

Locations

Hypocenters relocated after CDI are plotted in Figures 9 a and b. Many of the events are located beneath Kilauea caldera, though there is a distinct cluster to the southeast in the ERZ and a deeper cluster to the northwest near the edge of the Kaoiki fault zone. These clusters are presumably regions under high stress and/or composed of rock that is prone to brittle failure. About 40% of the events in the study occurred during a swarm on February 1, 1996, including almost all of the ERZ cluster. The upper ERZ is frequently the site of swarms, with durations on the order of a few days (Klein et al. 1987).

A comparison of hypocenters from Dawson et al. (1999) and from this study is shown in Figures 10 a and b. It is important to note that although both studies used data from the JUST experiment, the earthquake catalogs are not exactly the same. Most of the phases were picked independently, though some were provided by USGS scientists (P. Dawson, pers.com.). Data from the 1997 JUST experiment was used in only this study. Despite the difference in data sets, the seismicity patterns are similar. Most of the events are beneath the caldera, and the Kaoiki and ERZ clusters are both well defined. There is a subtle systematic difference in the location of the two clusters, however; events from this study are slightly deeper in the Kaoiki cluster and further east in the ERZ cluster.

The relocations from this study can also be compared to those from the HVO catalog, located using data from only the broad, sparse permanent HVO network

(Figures 11a,b). Though the data is from the same time period, the HVO catalog does not contain many of the smaller events that were located with the augmented JUST networks. The locations from this study appear to be systematically deeper, and the seismically active volumes are more well constrained. This is likely a result of the additional station coverage and the 3D velocity model.

P-Phase Velocity Structure

The Vp model is shown in selected depth sections (Figures 12a-l) and cross sections (Figures 13a-d). Depths indicated are below sea-level. It should be noted that the color scale is different for each figure. Change in Vp over the model is dominated by an increase with depth, so the colorscale must be "tuned" for each section to allow the clear definition of anomalies. This is especially important to consider when comparing a cross-section view of an anomaly to a depth section.

Near the surface (from -0.75 to 0 km), the most distinct feature is a high-Vp anomaly centered beneath Kilauea caldera at -0.25 km, but is most prevalent on the southwest edge of Kilauea caldera at -0.75 (Figures 12a,b). There is also a low-Vp anomaly that extends from Kilauea caldera to the southeast that is seen through several shallow layers (Figures 12a,b,c).

A second high-Vp anomaly, up to 2 km wide, extends from -0.25 to 2.75 km depth about 4 km southeast of Halemaumau crater (Figures 12b-h). This region closely coincides with the ERZ cluster (Figure 14a). The anomaly spreads to the west at 2.25 km depth, and merges with a much larger high-Vp anomaly in the center of the study

region (Figures 12g-l). The larger anomaly widens with depth, and it appears to extend below the study region south of Kilauea caldera.

A distinct low-Vp anomaly is centered to the southwest of Halemaumau crater at a depth of 0.25 km (Figure 12c). It extends up into the shallower layers to the west, south, and east, forming a partial "dish" ~5 km in diameter. This feature can be seen in Figures 14b and d, but it should be noted that the colorscale has been highly "tuned". This produced a false feature of low apparent Vp to the north and east of the "dish" anomaly. A larger, deeper low-Vp anomaly is found directly beneath (the top is at 0.25 km) and to the southwest of Halemaumau, extending below the "dish" anomaly. The region splits into two lobes around 1.75 km depth, the west lobe is seen down to 4.25 km, while the other, directly beneath Kilauea caldera, is not seen below 2.25 km (Figures 12d-k, 14c). Other high- and low-Vp regions are seen near the surface, but they are either near the edge of the imaged region and may be artifacts from the inversion, or they do not correlate well from layer to layer.

A histogram of normalized Vp from -0.75 to 3.25 km depth, where the Vp of each cell is divided by the mean Vp of its layer, shows a clear break in slope that separates the anomalously low Vp's from the background at 9% (Figure 15). The total volume of the cells in this anomalous portion is 26.2 km^3. Using a similar method (percentage deviation from the starting model), Dawson et al. (1999) calculated a low-Vp anomaly volume of 27 km^3. In both studies, these shallow low-Vp anomalies are interpreted to be the summit magma chamber. This result will be discussed below.

Vp/Vs Structure

The Vp/Vs model is shown in selected depth sections (Figures 16a-l) and cross sections (Figures 18a-c). It should be noted again that the color scale is different for each figure.

There are two distinct regions of high-Vp/Vs. One is ~4.5 km southeast of Halemaumau crater from 1.25 to 2.75 km depth, in the same region as the ERZ earthquake cluster and a high-Vp anomaly. Within this region there are three localized high-Vp/Vs anomalies, with values up to 2.7 (Figures 16e-h, 18a,b). These values are significantly different than the Vp/Vs = 1.77 in the starting model.

The other region is beneath Kilauea caldera from -0.25 to 1.75 km depth (Figures 16a-d, 18b,c). In detail, the region contains three high-Vp/Vs anomalies with values up to 2.6, spatially related to the earthquakes clustered beneath the summit as well as a low-Vp anomaly. One of the three distinct anomalies within the region lies almost directly beneath the east edge of Halemaumau at 0.75 km depth (Figures 16d, 18b).

The remaining high-Vp/Vs anomaly is seen 3 km southwest of Halemaumau at depth 2.25 km (Figure 16g). Other high-Vp/Vs regions are seen in the model, but they are either near the edge of the imaged region and may be artifacts from the inversion, or they do not correlate well from layer to layer.

Discussion

A comparison of the CDI Vp and Vp/Vs models (Figures 12a-l, 13, 14a-d, 16a-l, 17, 18a-c) with the least-squares starting model (Figures 8a-h) shows a marked improvement in image resolution. This is attributable in part to the finer grid spacing, but it is also clear that blurred images in the least-squares model have more sharply defined boundaries in the CDI model. Some of the features, including the large high-Vp anomaly in the ERZ to the southeast of the caldera, are not seen at all in the least-squares model. Clearly, CDI has improved on the least-squares model significantly.

There have been many previous tomography experiments at Kilauea to which the results of the current study can be compared. Thurber (1984), Rowan and Clayton (1993), Okubo et al. (1997), and Dawson et al. (1999) have all imaged high P-phase velocities in a region from 4 to 11 km deep, centered below the summit. The top of this body is seen in the lowest layers of the Vp model in this study, starting at 3.25 km depth (Figures 12g-l). Prior to this study, only in Dawson et al. (1999) and Thurber (1984) have low-Vp anomalies been imaged in the shallowest layers.

Dawson et al. (1999) show a low-Vp anomaly centered at a point 3 km to the southeast of Halemaumau crater. It is approximately 5 km in lateral extent, and it extends to a depth of 3 km. In their shallowest layer, from -1.0 to -0.5 km depth, the low Vp anomaly splits in two, one directly under the crater and another to the south. Thurber (1984) imaged a roughly spherical region 3 km in diameter and centered at 1 km depth beneath the summit that was interpreted to be the summit magma complex.

Although the low Vp anomalies occur in generally the same regions as in the model from this study, there are several important differences. There are low velocity anomalies in the layers above sea level, however, the largest does not appear until 0.25 km depth (Figures 12d-k, 14c). It is in general smaller and to the west of the anomaly in Dawson et al. (1999) and Thurber (1984). At 1.25 km depth, the CDI anomaly splits into two lobes. The hotspot that formed the Kilauea volcano is moving southeast relative to the island (MacDonald, 1986). It is possible that the western lobe of the large low-Vp anomaly is trace of an earlier plumbing system.

As noted above, the anomalously low Vp volume in the top 4 km of the model is 9% or slower than background. This compares favorably to the anomalous Vp values found in Dawson et al. (1999), which were up to 10% of background. Theoretical calculations of the acoustic properties of partially molten material indicate that Vp perturbation of approximately 1% is equivalent to a 1% volume fraction of mafic melt, over a range of up to ~10%. (Takei, 1998) Therefore, if the shallow low Vp anomalous volume (26.2 km^3) is the summit magma chamber, it is composed of ~9%, or 2.4 km^3, of mafic melt. This volume compares well to previous estimates of active chamber volume: ~2-3 km^3, based on a recent analysis of the residence time of geochemical fluctuations (Pietruszka and Garcia, 1999); and ~2-13 km^3, from the modeling of post-eruptive subsidence from geodetic and gravity data (Johnson, 1992).

The "dish" shaped low-Vp anomaly imaged above -0.25 km (Figures 12d-k, 14c) may be associated with a ring fracture system as well as thick ash and tephra deposits to the south of the caldera (Dawson et al., 1999). Based on studies of

weathering, the crust to the northwest of the caldera is the oldest in the study area (Holcomb, 1987). The small low Vp anomaly below the northwest edge of the caldera may be a result of this geology (Figure 12a).

The two high Vp anomalies that extend to the top of the model below the caldera can be attributed to ponded lava flows. In the inversion, Vp is imaged to within ~250 m of the caldera floor. It is likely that the high Vp would extend almost to the surface.

An anomaly that does not appear in Dawson et al. (1999) is the large high-Vp anomaly that coincides with the ERZ cluster 4.5 km to the southeast of Halemaumau, extending from 0.25 to 2.25 km in depth (Figures 12b-h). Dawson et al. (1999) image this region as a low-Vp anomaly. There are three small high-Vp/Vs anomalies within the region defined by the earthquake cluster (Figures 16e-h, 18a,b), which do agree with the results of Dawson et al. (1999). As with the anomaly just below the caldera floor, high P-phase velocities are typically associated with more solid, denser material, such as lava flows. The Vp/Vs ratio (2.7) of two of the small anomalies within the region corresponds to a Poisson's ratio of 0.42. This high value strongly suggests the presence of highly fractured rock, gas, and/or partial melt. The presence of the earthquake cluster also suggests the brittle fracturing of material. This evidence, and its location within the ERZ indicates that the region defined by the earthquake cluster is a cooled magma chamber. The small Vp/Vs anomalies within the region may be pockets of highly fractured material.

Other high-Vp/Vs anomalies in the CDI model also appear in generally the same regions as the two large lobes of high Vp/Vs imaged in Dawson et al. (1999). The ~1 km diameter lobes are centered 1 and 2 km beneath points 2 km southwest and southeast of Halemaumau, respectively (Dawson et al., 1999). The CDI anomaly 3 km southwest of Halemaumau at depth 2.25 km (Figure 16g) coincides with the bottom of the western lobe of the anomaly seen in Dawson et al. (1999).

The high-Vp/Vs regions below Kilauea caldera (Figures 16e-h, 18b,c) closely coincide with earthquake clusters. The region also coincides with the summit magma reservoir interpreted from tilt measurements (Dvorak and Okamura, 1987). Given the known presence of magma below Kilauea caldera, the high-Vp/Vs anomalies may define pockets of partial melt or exsolved gases within the summit magma complex.

Within this region, a distinct anomaly beneath Halemaumau at 0.75 km depth (Figures 16d, 18b) coincides with the northeastern lobe of the large low-Vp anomaly (Figures 12d-f). It also correlates well with a similar small anomaly seen from 0.0 to 0.5 km depth in the Dawson et al. (1999) study, and it is at the center of the low Vp anomaly imaged in Thurber (1984). Dawson et al. (1999) interpreted this anomaly to be the "bridge" between the two large lobes of high Vp/Vs. Further, this high-Vp/Vs anomaly is colocated with the source of very long period impulsive signals recorded during the February 1, 1996 swarm (Ohminato et al., 1998). The results of a waveform inversion of these signals are consistent with a crack-like source acting as a buffer to the flow of magma to the ERZ. The movement of magma through this crack could involve a large slug of exsolved gas from the summit reservoir (Ohminato et al., 1998).

The difference in size and shape of the largest low Vp anomaly between this study and Dawson et al. (1999) is likely the result of our more evenly distributed ray coverage and a tomography algorithm (CDI) designed to image distinct anomalies. The number of earthquakes and the number of arrivals in the two studies are similar (271 earthquakes and 8246 arrivals in this study versus 206 earthquakes and 7890 arrivals in Dawson et al. (1999)), but the arrivals were in this study were recorded over two recording periods (January 1996 and February 1997) at a total of 249 stations, compared to 67 in Dawson et al. (1999).

Conclusions

The inversion of P-phase velocity and Vp/Vs ratio have shown a complex summit magma system. The anomalies inferred to be chambers of partial melt or concentrations of exsolved gases occur in the same place as seen in previous studies, and their presence correlates with tilt data.

The Hawaiian volcanoes, particularly Kilauea, have been the site of numerous tomographic studies. Each successive experiment has improved on the previous ones, in terms of the methods, grid spacing, and the resulting images. Here, a new tomography algorithm, CDI, has been applied successfully to a large and spatially well-distributed data set. The ray coverage allowed for a finer grid spacing (250 m) than in previous studies. The spatially distinct, high value anomalies imaged will provide better constraints on models of volcanic processes, for example the magma injection associated with the February 1, 1996 swarm.

References

Aki, K., A. Christoffersson, E.S. Husebye, Determination of the three-dimensional seismic structure of the lithosphere, *J. of Geophy. Res.*, 82, 2, 277-296, 1977

Benz, H.M., B.A. Chouet, P.B. Dawson, J.C. Lahr, R.A. Page, J.A. Hole, Three-dimensional P and S wave velocity structure of Redoubt Volcano, Alaska, *J. of Geophys. Res.*, 101, 8111-8128, 1996.

Clippard, J.D., Advancements in seismic tomography with application to tunnel detection and volcano imaging, *PhD Dissertation, University of Alaska Fairbanks*, 1998.

Clippard, J.D., D.H. Christensen, R.D. Rechtien, Composite distribution inversion applied to crosshole tomography, *Geophysics*, 60, 1283-1294, 1995.

Dawson, P.B., B.A. Chouet, P. Okubo, A. Villasenor, H.M. Benz, Three-dimensional velocity structure of the Kilauea caldera, Hawaii, *Geophys. Res. Let.*, 26, 18, 2805-2808, 1999.

Dvorak, J.J., A.T. Okamura, A hydraulic model to explain variations in summit tilt rate at Kilauea and Mauna Loa Volcanoes, *U.S. Geological Survey Prof. Pap. 1350*, 1281-1296, 1987.

Eaton, J.P., K.J. Murata, How volcanoes grow, *Science*, 132, 925-938, 1960.

Ellsworth, W.L., R.Y. Koyanagi, Three-dimensional crust and mantle structure of Kilauea Volcano, Hawaii, *J. of Geophys. Res.*, 82, 33, 5379-5394, 1977.

Fiske, R.S., W.T. Kinoshita, Inflation of Kilauea Volcano prior to its 1967-1968 eruption, *Science*, 165, 3891, p. 341-349, 1969.

Hawaiian Volcano Observatory (Ed.). (1999, July 12 - last update). Summary of the Pu'u 'O'o - Kupaianaha Eruption, 1983-present. Homepage of the Hawaiian Volcano Observatory, Online. *Available: http://www.hvo.wr.usgs.gov/kilauea/summary/main.html,* 1999, Oct.15.

Heliker, C.C., M.T. Mangan, T.N. Mattox, J.P. Kauahikaua, R.T. Helz, The character of Long-term eruptions: inferences from episode 50-53 of the Pu'u 'O'o-Kupaianaha eruption of Kilauea Volcano, *Bull. Volcanol.*, 59, 381-393, 1998.

Hill, D.P., J.J. Zucca, Geophysical constraints on the structure of Kilauea and Mauna Loa volcanoes and some implications for seismomagmatic process, *U.S. Geological Survey Prof. Pap. 1350*, 903-917, 1987.

Holcomb, R.T., The eruptive history and long-term behavior of Kilauea Volcano, *U.S. Geological Survey Prof. Pap. 1350*, 261-350, 1987.

Jaggar, T.A., R.H. Finch, Tilt records for thirteen years at the Hawaiian Volcano Observatory, *Bull. Seismol. Soc. Am.*,19, 38-51, 1929.

Johnson, D.J., Dynamics of magma storage in the summit reservoir of Kilauea Volcano, Hawaii, *J. of Geophys. Res.*, 97, 82, 1807-1820, 1992.

Klein, F.W., A linear gradient crustal model for south Hawaii, *Bull. Seismol. Soc. Am.*, 71, 5, 1503-1510, 1981

Klein, F.W., Patterns of historical eruptions at Hawaiian volcanoes, *J. of Volc. and Geotherm. Res.*, 12, p. 1-35, 1982

Klein, F.W., R.Y. Koyanagi, Hawaiian Volcano Observatory seismic network history 1950-1979, *U.S. Geol. Surv. Open File Rep.*, 80-302, 1980

Klein, F.W., R.Y. Koyanagi, J.S. Nakata, W.R. Tanigawa, The seismicity of Kilauea's magma system, *U.S. Geological Survey Prof. Pap. 1350*, 1019-1186, 1987.

Klimes, L., M. Kvasnicka, 3-D network ray tracing, *Geophys. J. Int.*, 116, 726-738, 1994.

Koyanagi, R.Y., B. Chouet, K. Aki, Origin of volcanic tremor in Hawaii: Data from the Hawaiian Volcano Observatory, *U.S. Geological Survey Prof. Pap.* 1350, 1221-1257, 1987.

Macdonald, G.A., A.T. Abbott, F.L. Peterson, Volcanoes in the Sea: The Geology of Hawaii, *Honolulu, University of Hawaii Press*, 2nd edition, 80-81, 1986.

McNutt, S.R., Y. Ida, B.A. Chouet, P. Okubo, J. Oikawa, G. Saccorotti, Kilauea Volcano provides hot seismic data for joint Japanese-U.S. experiment, *EOS*, 78, 10, p. 105, 111, 1997.

McNutt, S.R., Seismic monitoring and eruption forecasting of volcanoes: a review of the state-of-the-art and case histories, *Monitoring and Mitigation of Vol. Hazards*, 99-145, 1996.

Mogi, K., Relations between the eruptions of various volcanoes and the deformation of the ground around them, *Bull of the Earthquake Res Inst.*, Univ of Tokyo, 36, 1958

Okubo, P.G., H.M. Benz, B.A. Chouet, Imaging the crustal sources beneath Mauna Loa and Kilauea volcanoes, Hawaii, *Geology*, 25, 867-870, 1997.

Okubo, P.G., J. Nakata, B. Chouet, P. Dawson, The February 1, 1996 Kilauea summit earthquake swarm [abs.], *EOS*, 77, 46, F798, 1996.

Ohminato, T., Chouet, B.A., Dawson, P., Kedar, S., Waveform inversion of very long period impulsive signals associated with magmatic injection beneath Kilauea Volcano, Hawaii, *J. of Geophys. Res.*, 103, B10, 23839-23862, 1998.

Paige, C.C., M.A. Saunders, LSQR: An algorithm for sparse linear equations and sparse least squares, *ACM Transactions on Mathematical Software*, 8, 43-71, 1982.

Pietruszka, A.J., M.O. Garcia, The size and shape of Kilauea Volcano's summit magma storage reservoir: a geochemical probe, *Earth and Plan. Sci. Lett.*, 167, p. 311-320, 1999.

Quinlan, D. M. (Ed.). (1998, Nov. 30 - last update). A Tutorial for Datascope: the ASIS Relational Database System, Homepage of Boulder Real Time Technologies, Online. *Available: http//www.brtt.com/datascope/datascope.html*, 1999, September 8.

Rowan, L.R., Clayton. R.W., The three-dimensional structure of Kilauea Volcano, Hawaii, from traveltime tomography, *J. Geophys. Res.*, 98, 4355-4375, 1993.

Ryan, M.P., R.Y. Koyanagi, R.S. Fiske, Modeling the three-dimensional structure of macroscopic magma transport systems: Applications to Kilauea Volcano, Hawaii, *J. Geophys. Res.*, 86, 711-7129, 1981.

Smith, R.L., Ash flows, *Bull. of the Geol. Soc. of Am.*, 71, 795-842, 1960.

Swanson, D.A., D.B. Jackson, R.Y. Koyanagi, T.L. Wright, The February 1969 east rift eruption of Kilauea Volcano, Hawaii, *U.S. Geol. Surv. Prof. Pap., 1056*, 55 pp., 1979.

Takasaki, K.J., G.T. Hirashima, E.R. Lubke, Water resources of windward Oahu, Hawaii, *U.S. Geol. Surv. Prof. Pap., 1894*, 119 p., 3 pls. in pocket, 1969.

Takei, Y., Constitutive mechanical relations of solid-liquid composites in terms of grain-boundary contiguity, *J. Geophys. Res.*, 103, 18183-18203, 1998.

Thornber, C.R., D. Sherrod, C. Heliker, J. Kauahikaua, F. Trusdell, M. Lisowski, P. Okubo, Kilauea's ongoing eruption: Napau crater revisited after 14 years [abs.], *EOS*, 78, 17, p. S329, 1997.

Thurber, C.H., Seismic detection of the summit magma complex of Kilauea Volcano, Hawaii, *Science*, 223, 165-167, 1984.

Um, J., C. Thurber, A fast algorithm for two-point seismic ray tracing, *Bull. Seismol. Soc. Am.*, 77, 3, 972-986, 1987.

Yang, X., P.M. Davis, P.T. Delaney, A.T. Okamura, Geodetic analysis of dike intrusion and motion of the magma reservoir beneath the summit of Kilauea Volcano, Hawaii: 1970-1985, *J. Geophys. Res.*, 97, 3305-3324, 1992.

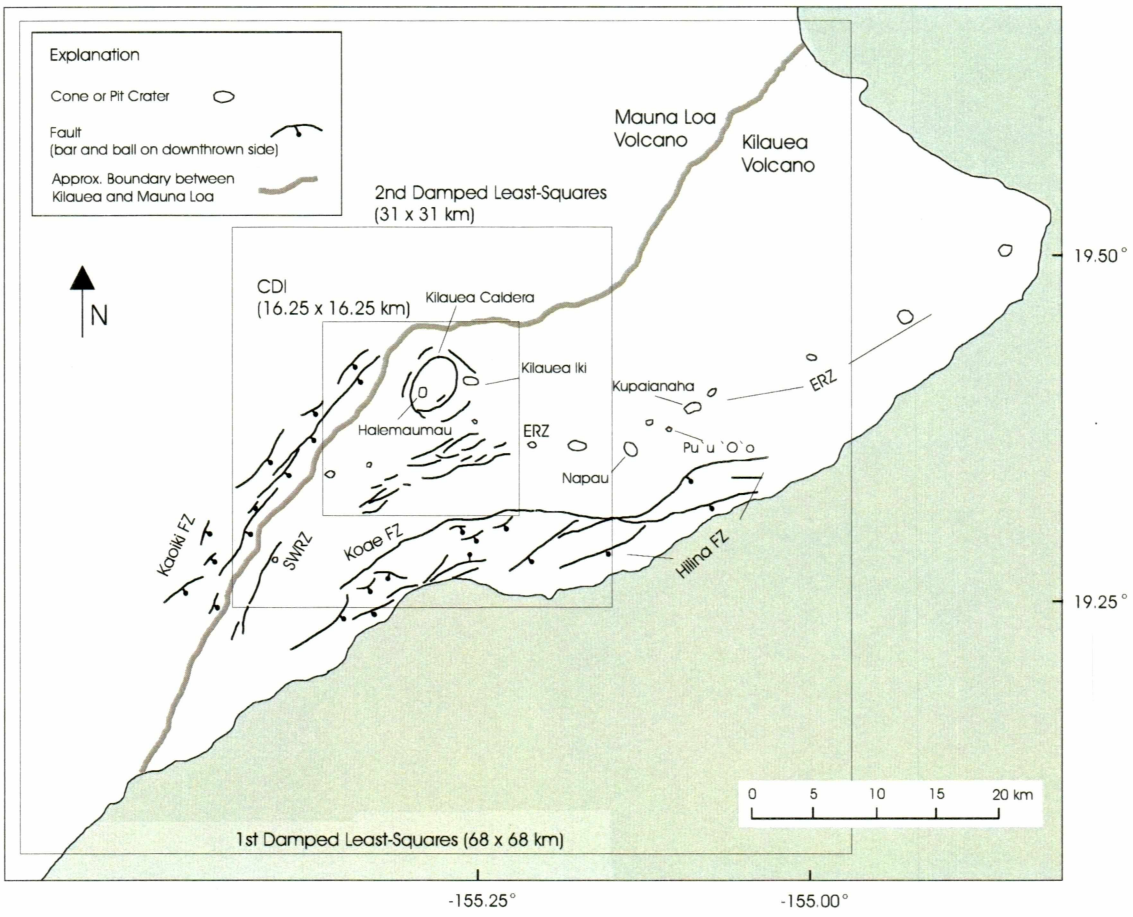

Figure 1: Map of Kilauea Volcano and the adjacent part of Mauna Loa Volcano. Structural regions discussed in this paper are labeled, and the study areas are shown. Map modified from Rowan and Clayton, 1993.

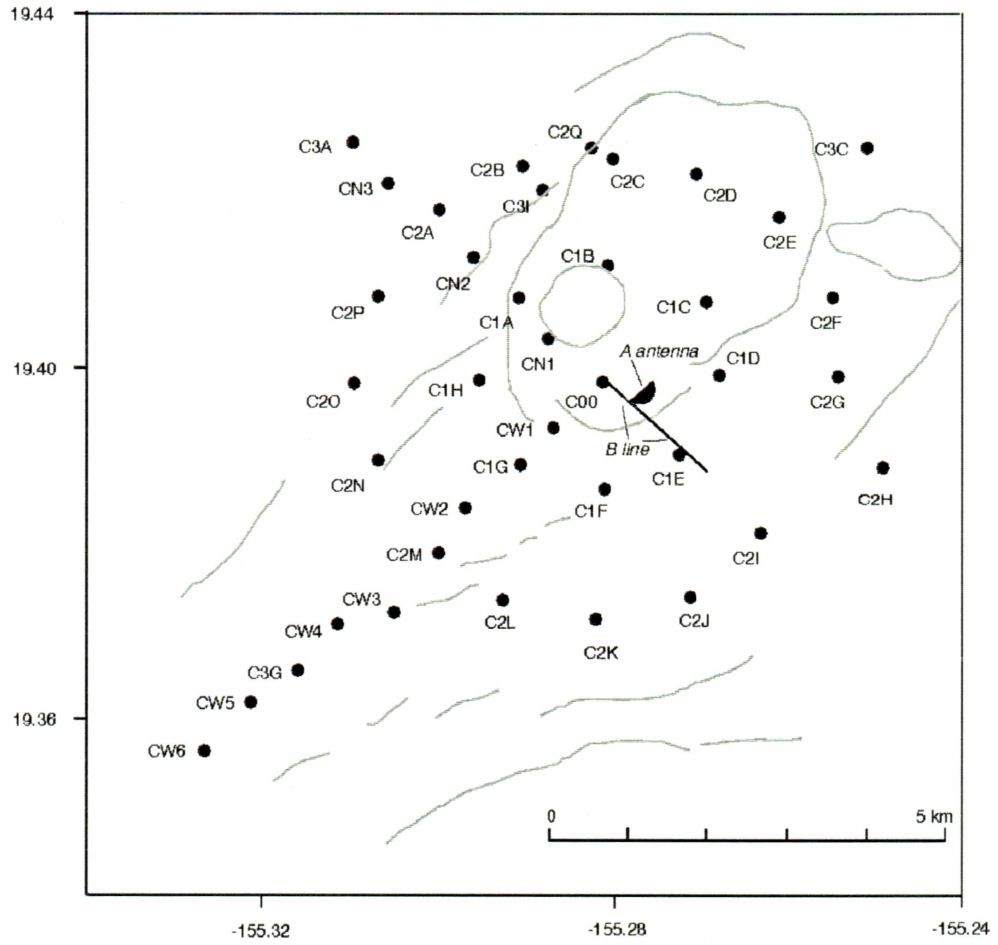

Figure 2: Map of the entire 1996 portable seismic network, including outlines of Kilauea caldera and Halemaumau crater, and positions of major faults. Each dot marks the position of a seismic station. See Figure 3 for an enlargement of the "A-antenna" and "B-Line".

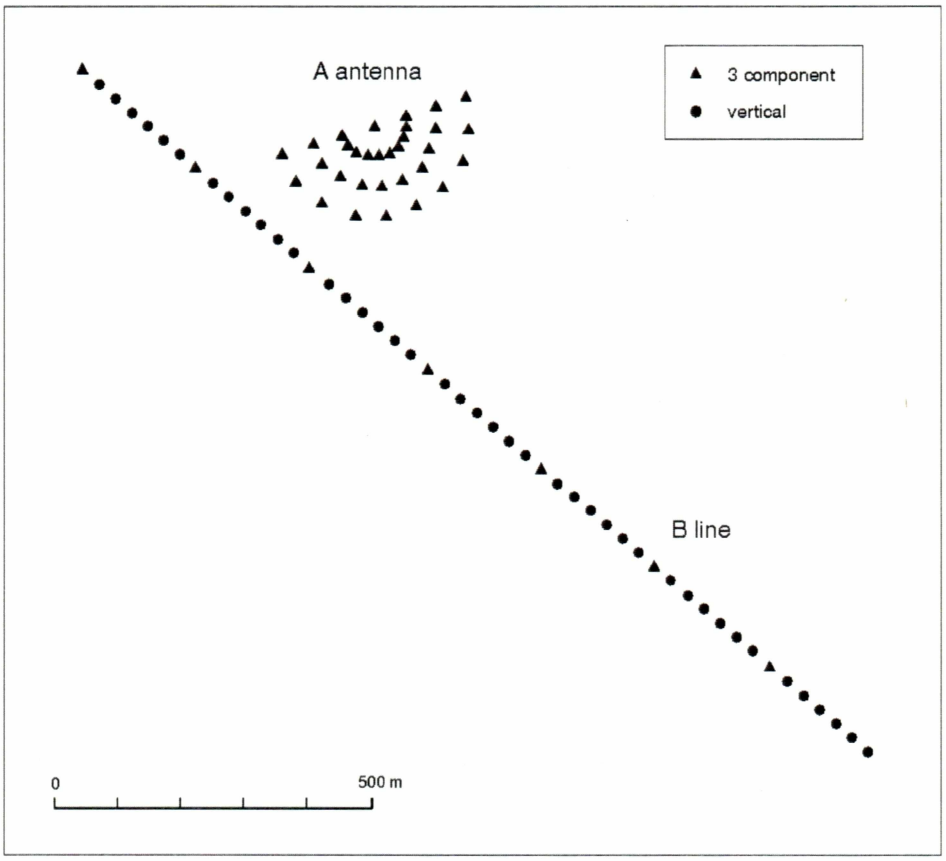

Figure 3: Map of the "A" antenna and the "B" linear array. See Figure 2 for general location information.

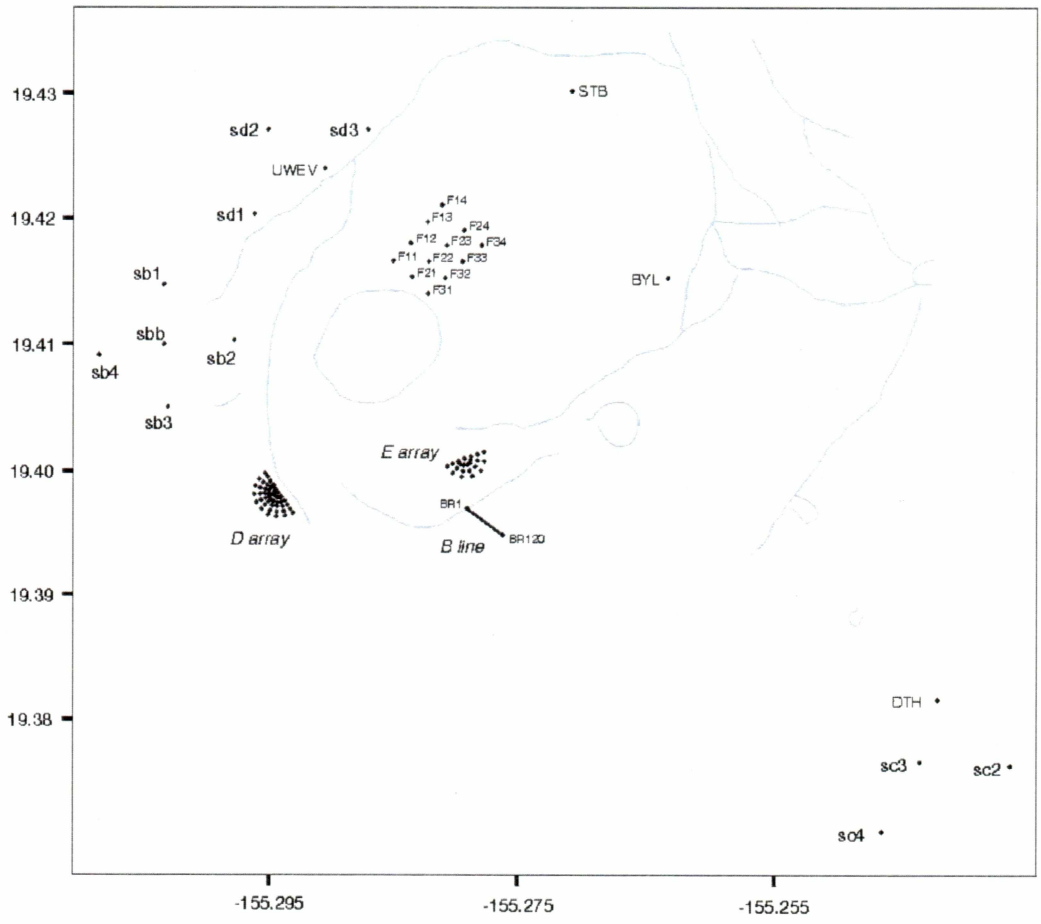

Figure 4: Map of the 1997 seismic network, including outlines of Kilauea caldera and Halemaumau crater, and positions of major faults. Each dot marks the position of a seismic station. Stations SBB, STB, BYL, DTH, F21 and UWEV are broadband stations.

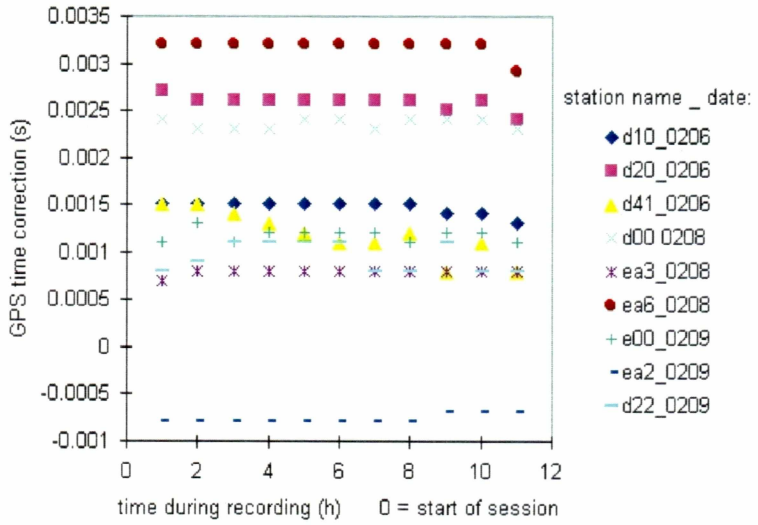

Figure 5: Hourly GPS time corrections for a sample of the 1997 recording sessions. Note that the correction is relatively constant over each session, indicating a nearly constant clock drift.

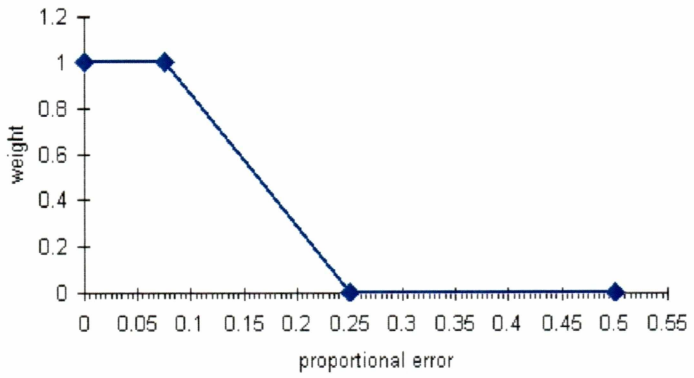

Figure 6: P- and S- phase arrivals weighted by proportional error (residual/ travel time). Full weight is given to arrivals with a proportional error <0.075, zero weight is given to those with errors >0.25.

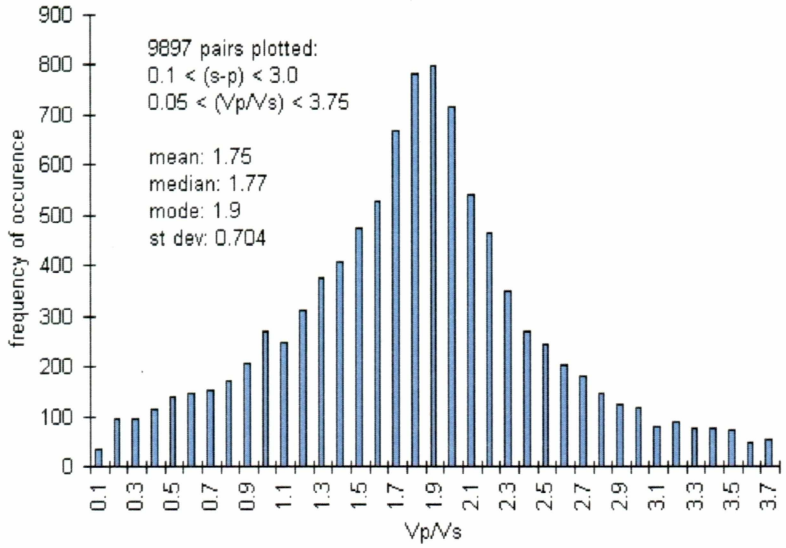

Figure 7: Histogram showing the distribution of the Vp/Vs ratio determined by the method described in Clippard (1998).

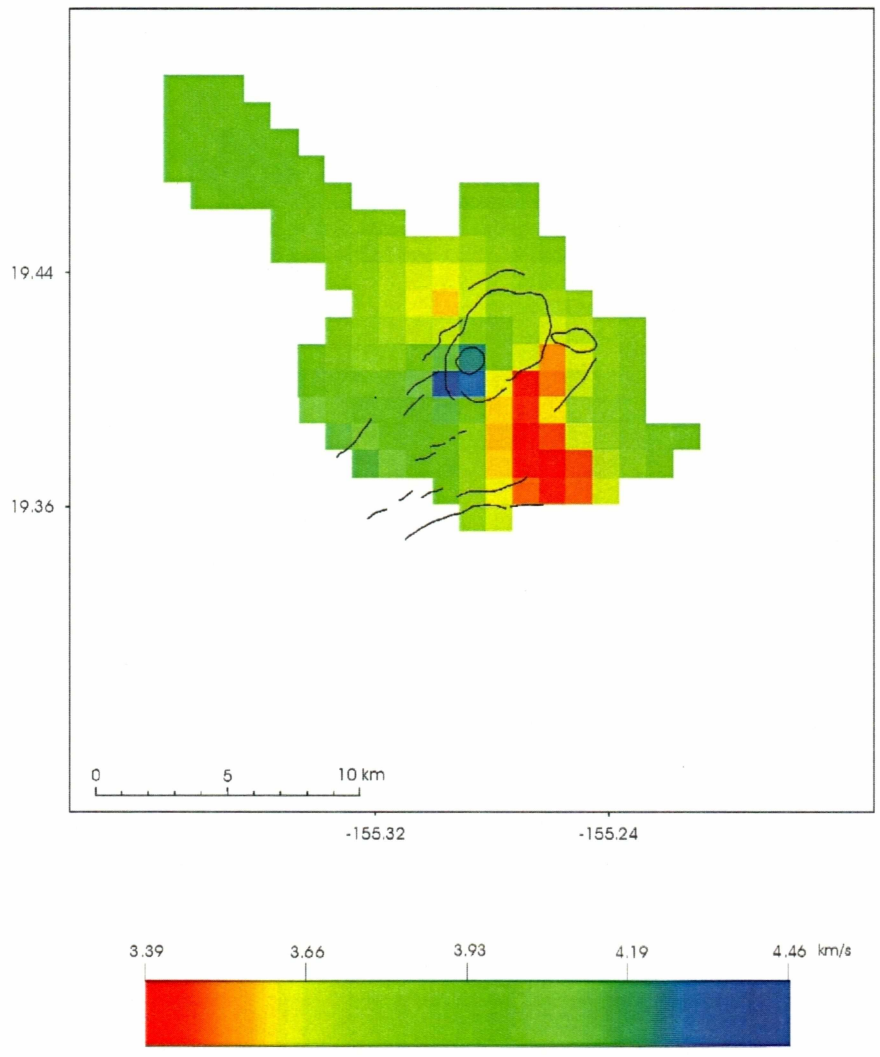

Figure 8a-h: 3D damped least-squares Vp and Vp/Vs model depth sections. A smoother version of this model was used as the input for CDI. The outline of Kilauea caldera, Halemaumau crater, and some of the faults are also shown. Depth in each figure is relative to sea level, positive downward

Figure 8a: Vp model, depth is -1.0 km.

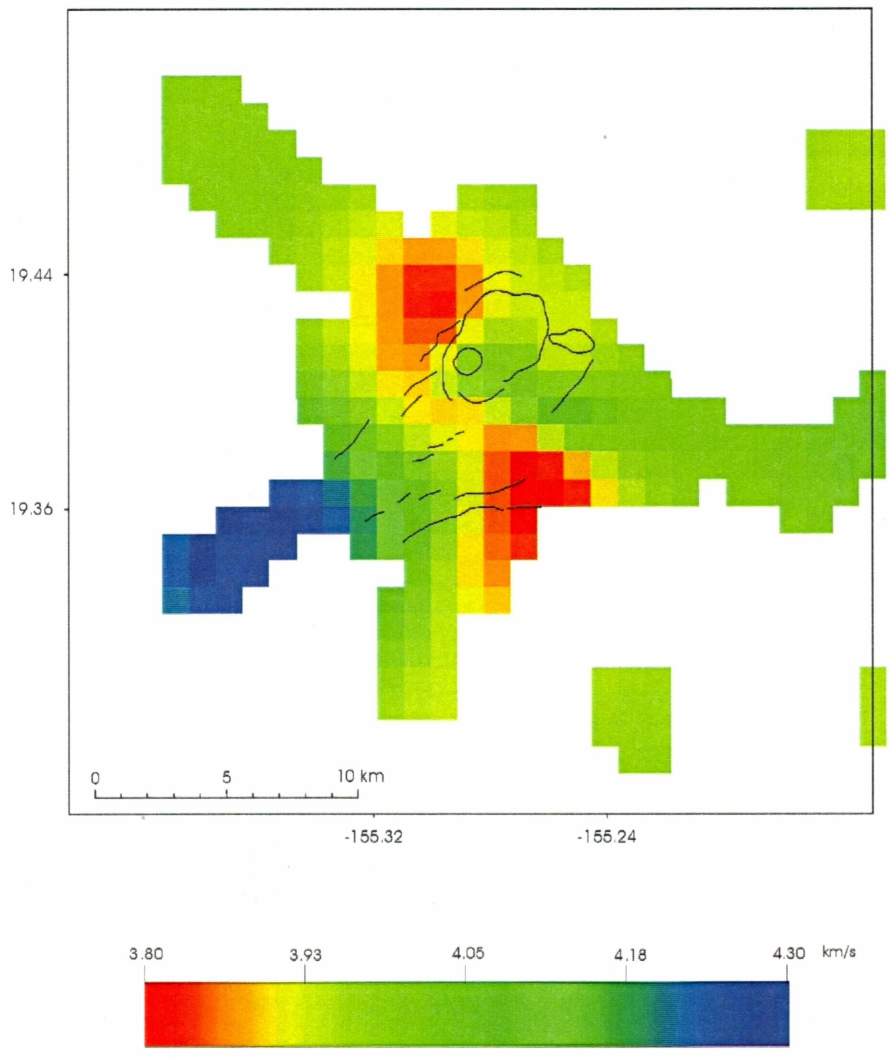

Figure 8b: Vp model, depth is 0 km.

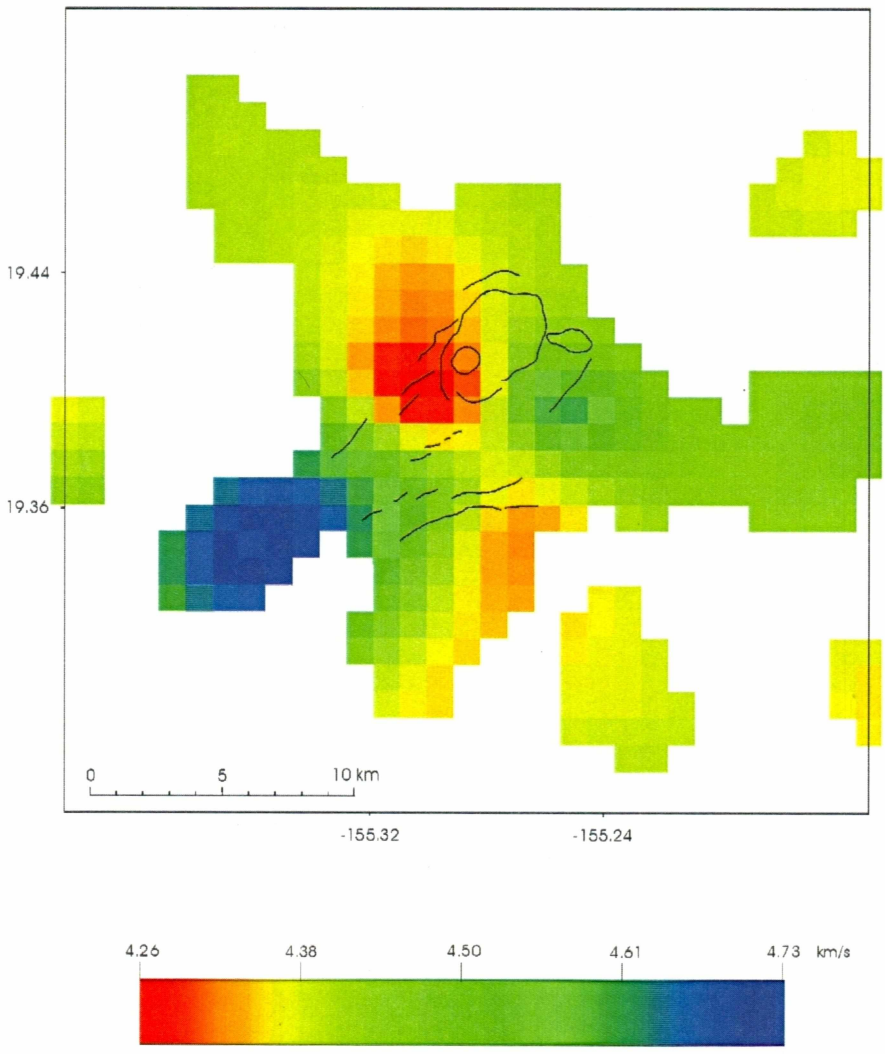

Figure 8c: Vp model, depth is 1.0 km.

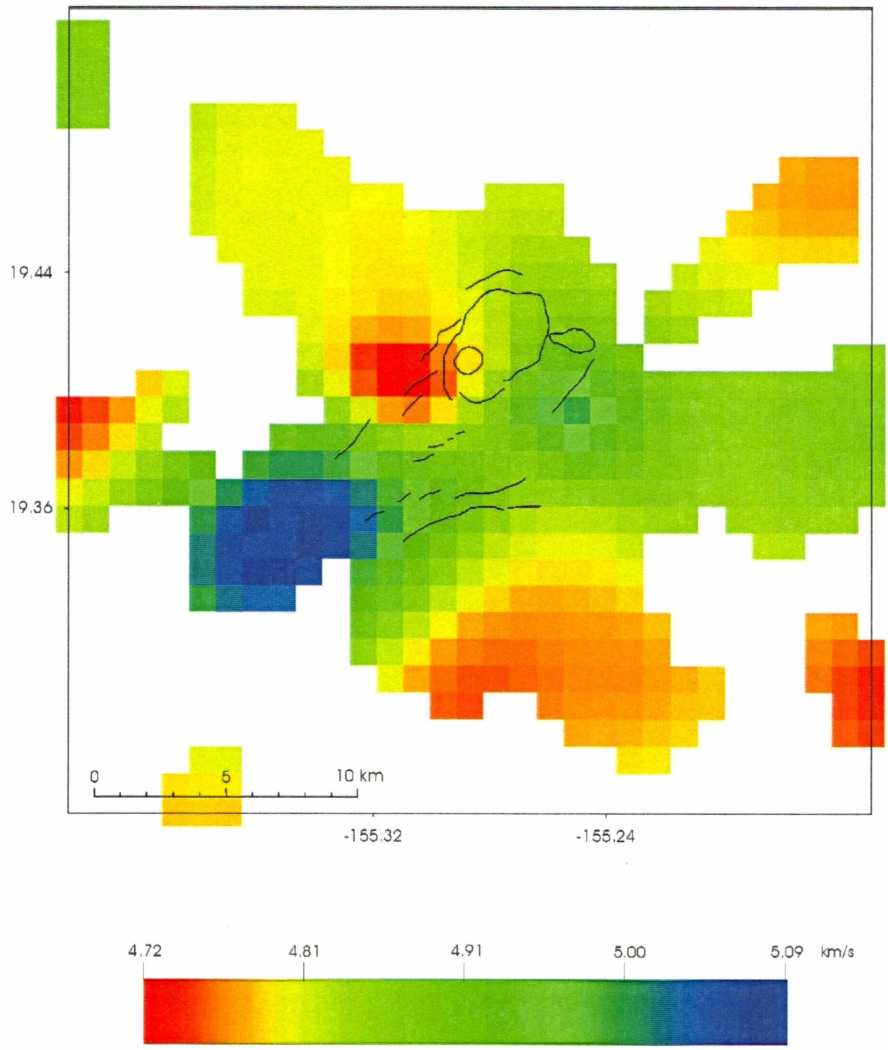

Figure 8d: Vp model, depth is 2.0 km.

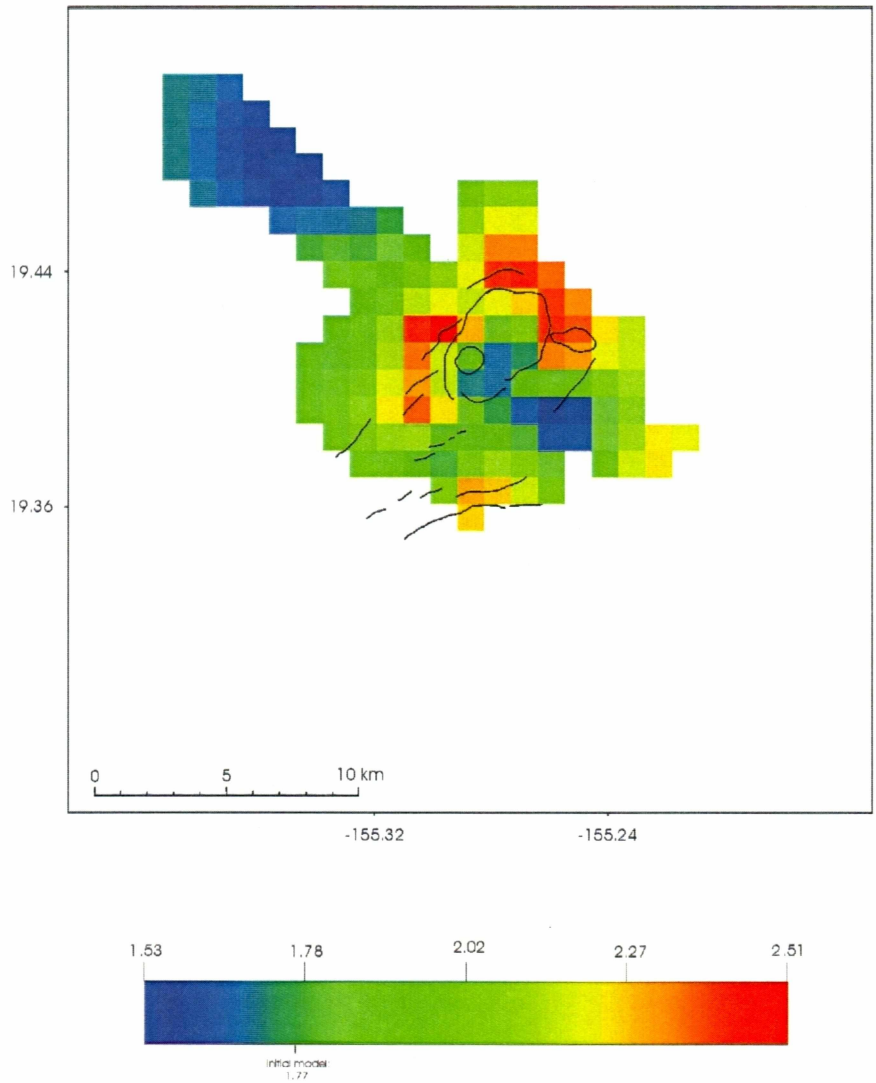

Figure 8e: Vp/Vs model, depth is -1.0 km.

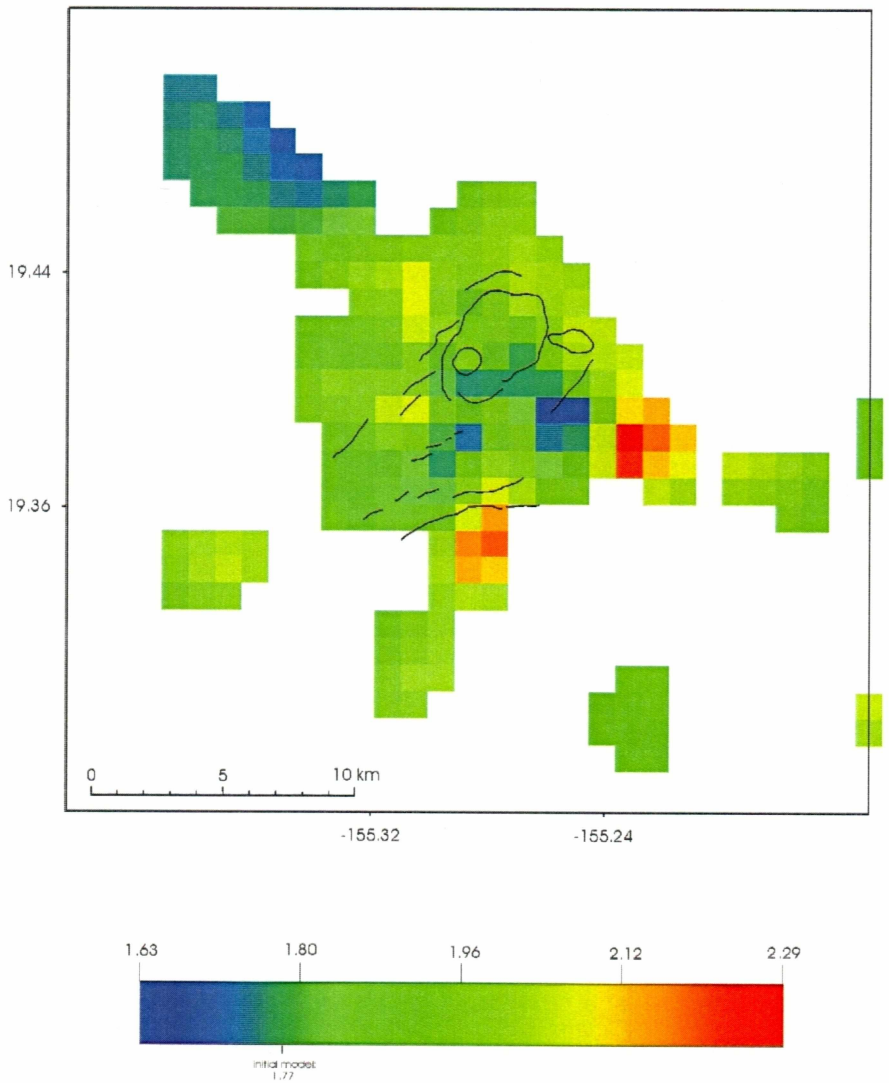

Figure 8f: Vp/Vs model, depth is 0 km.

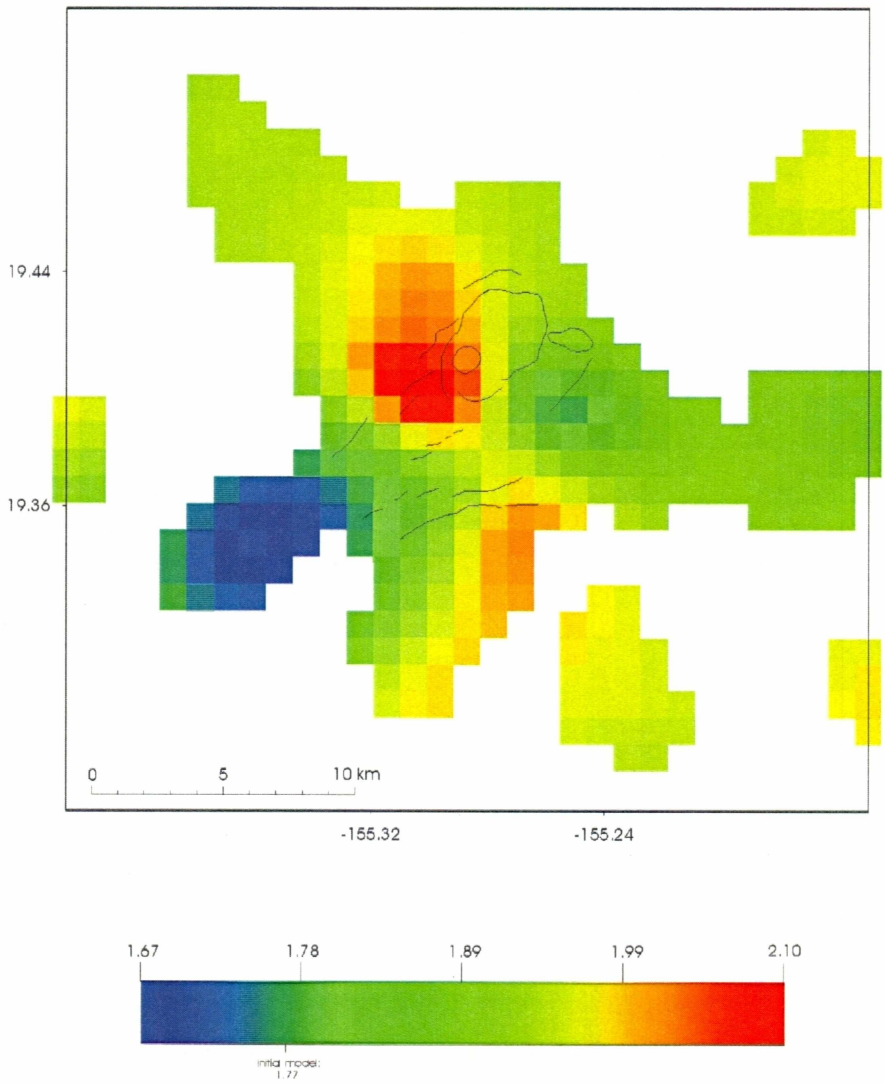

Figure 8g: Vp/Vs model, depth is 1 km.

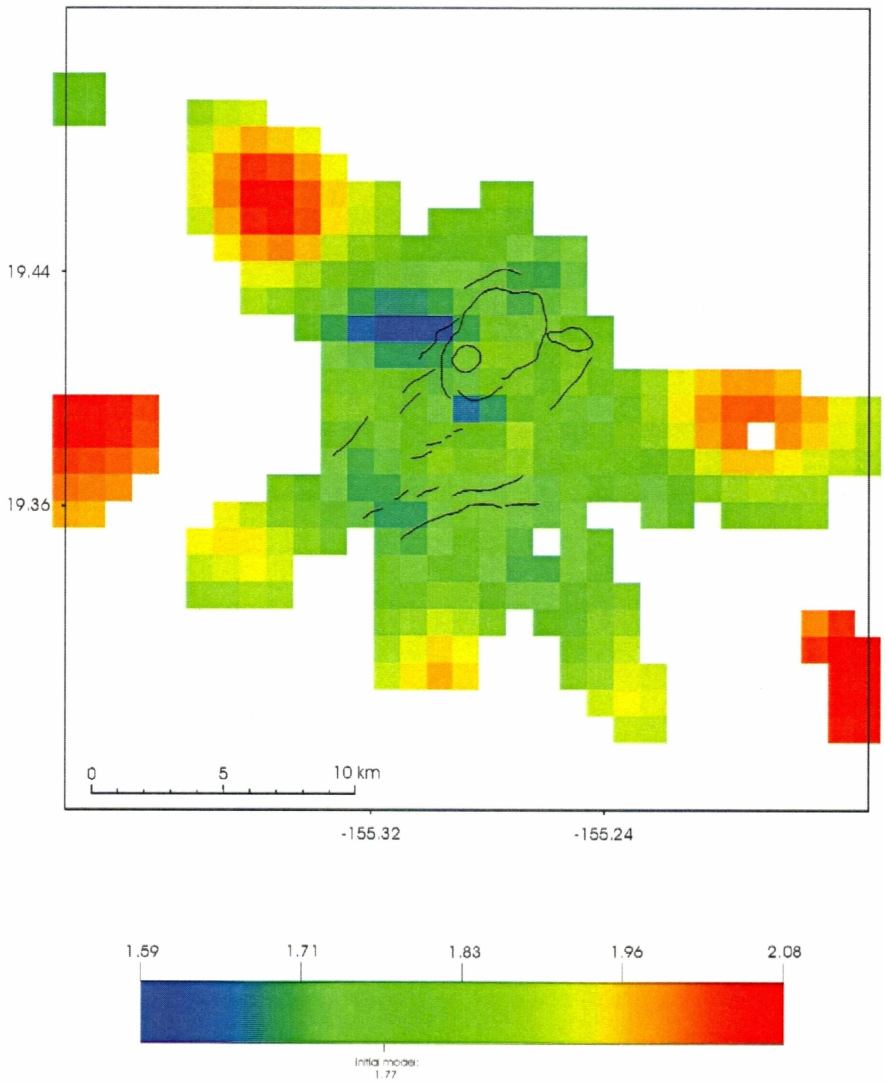

Figure 8h: Vp/Vs model, depth is 2 km.

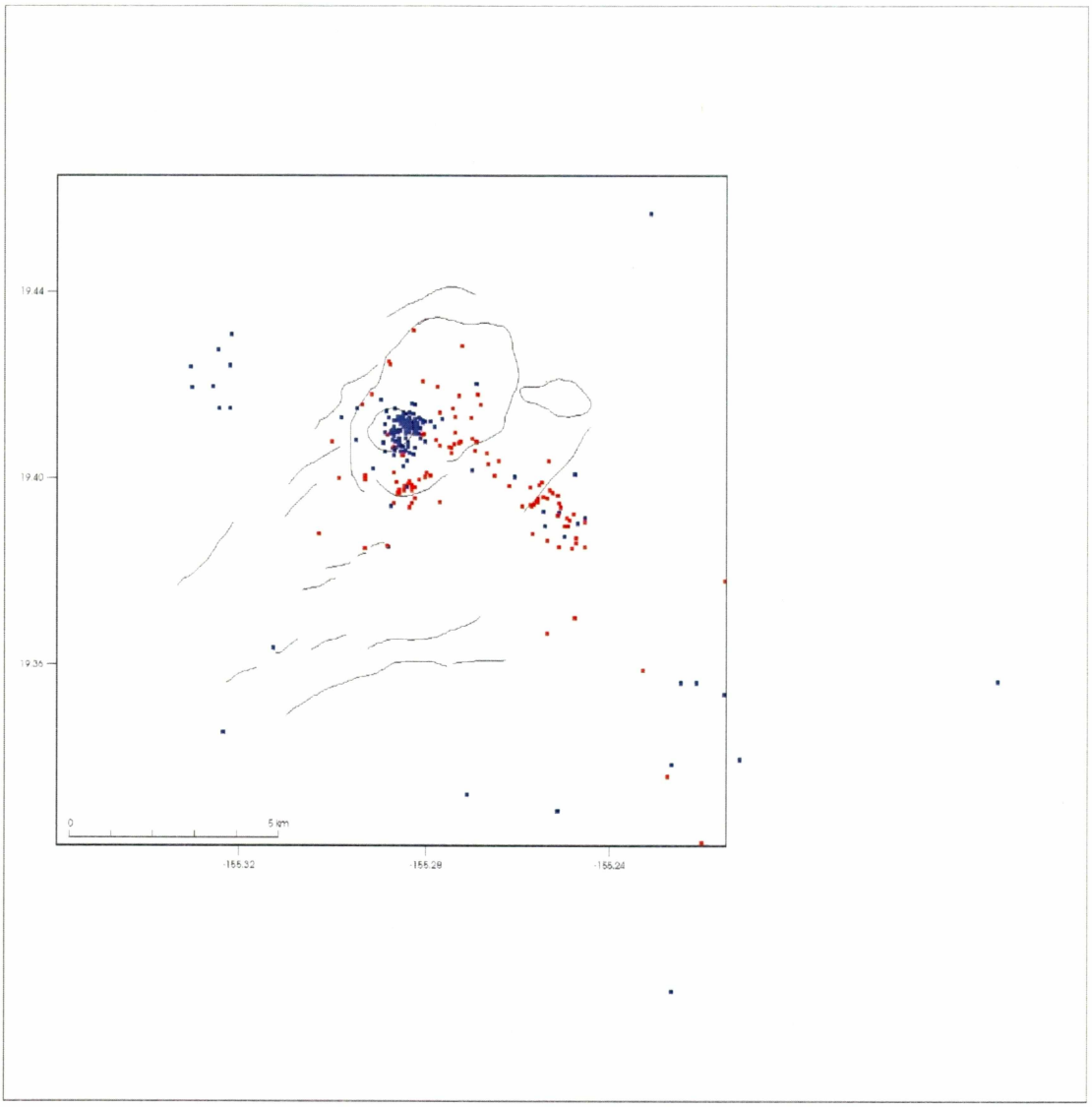

Figure 9a: Final locations of earthquakes after CDI, including the February 1, 1996 swarm (red squares). The inset shows the CDI study area. Map view.

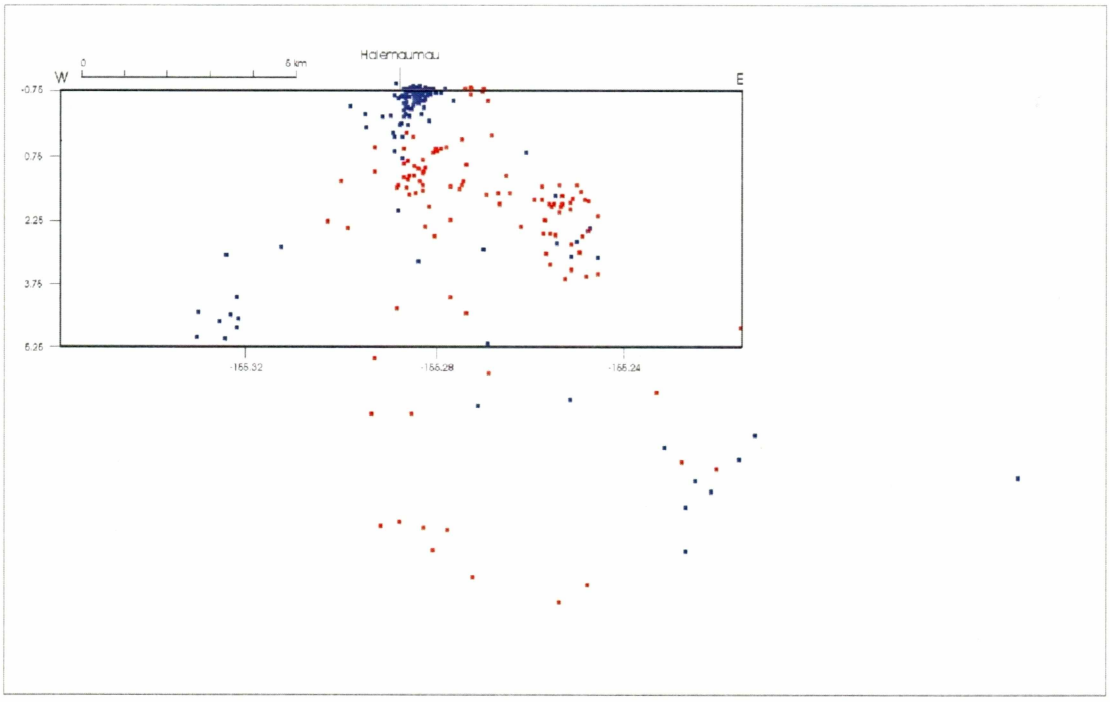

Figure 9b: Final locations of earthquakes after CDI, including the February 1, 1996 swarm (red squares). The inset shows the CDI study area. Side view, looking north.

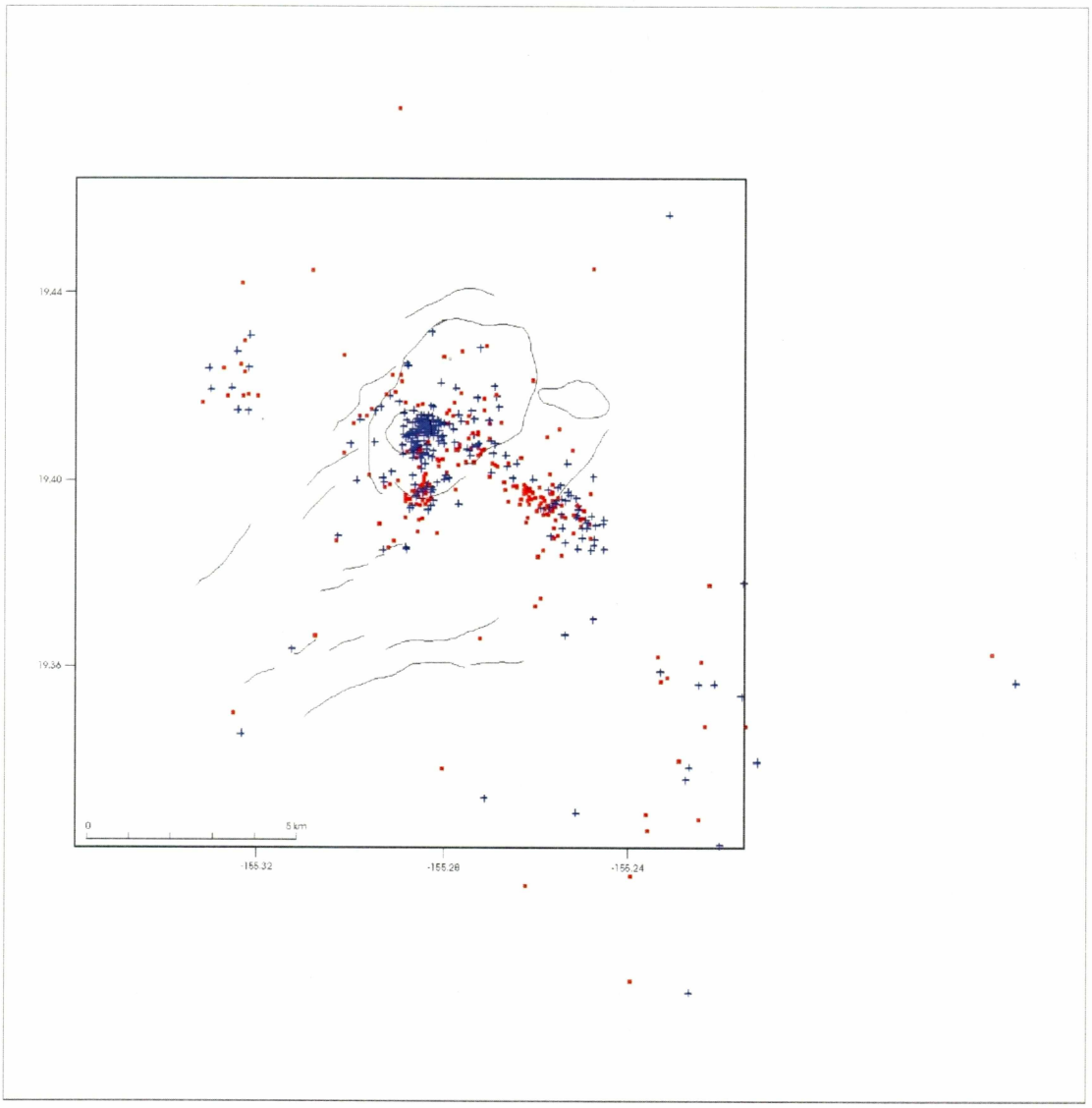

Figure 10a: Comparison of Dawson et al. (1999) hypocentral locations (red squares) with those after the final inversion (CDI) of this study (blue crosses). The inset shows the CDI study area. Map view.

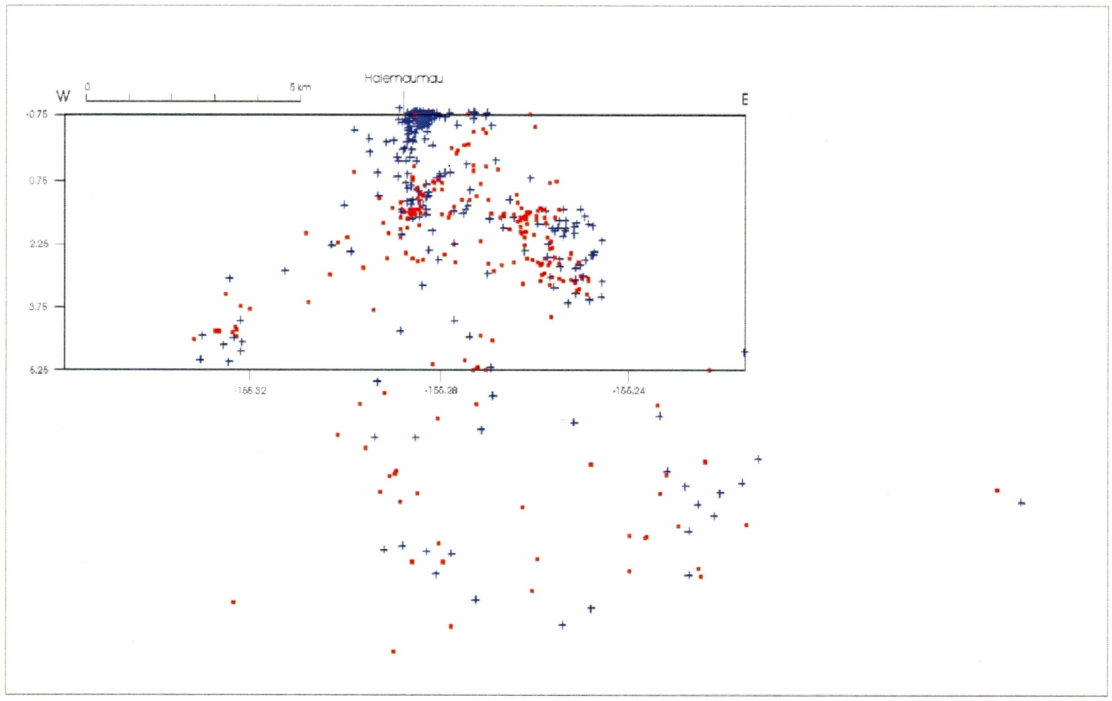

Figure 10b: Comparison of Dawson et al. (1999) hypocentral locations (red squares) with those after the final inversion (CDI) of this study (blue crosses). The inset shows the CDI study area. Side view, looking north.

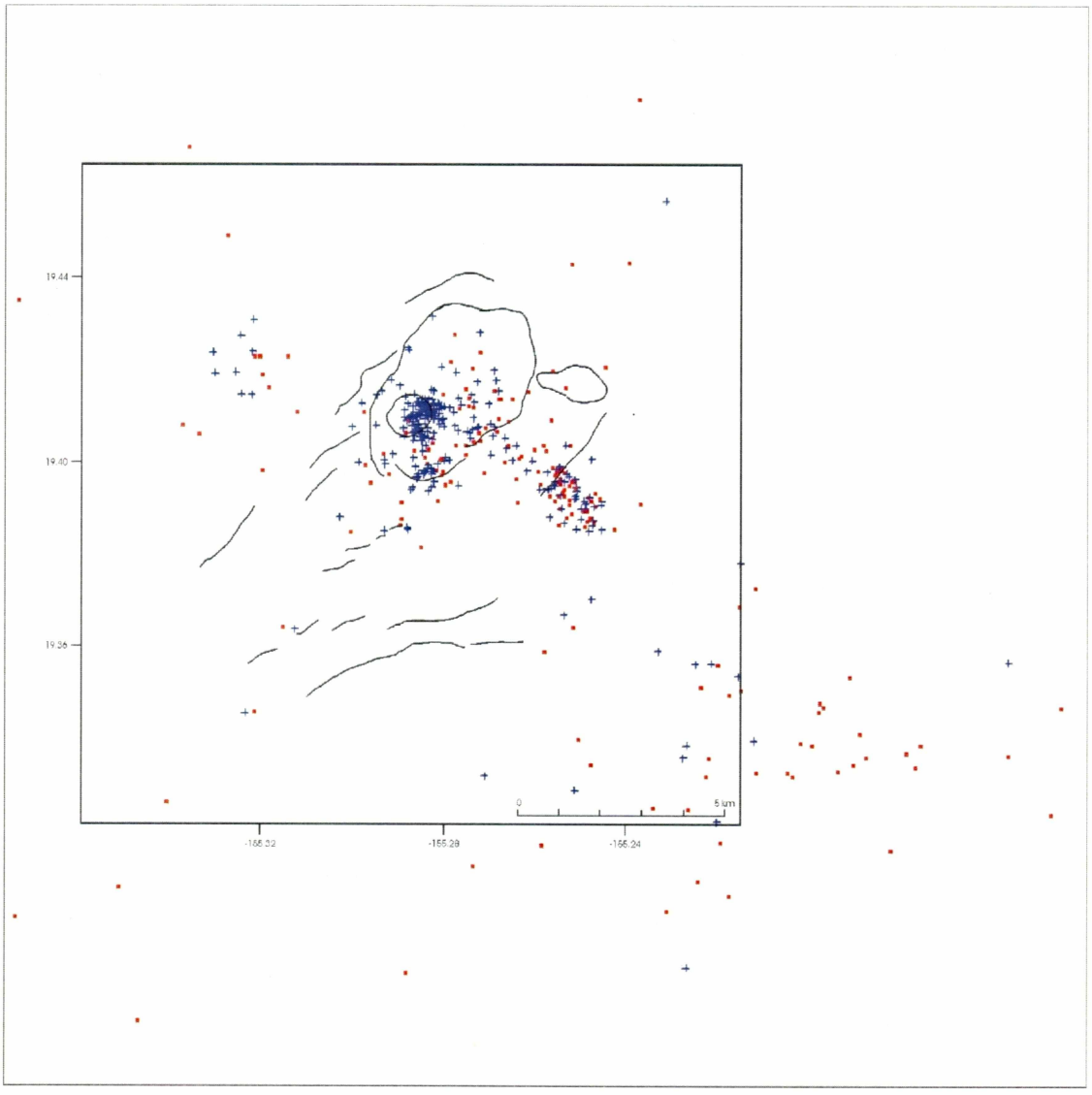

Figure11a: Comparison of HVO hypocenters from the same time period as the JUST 1996 experiment (red squares) with those from the final inversion (CDI) of this study (blue crosses). The inset shows the CDI study area. Map view.

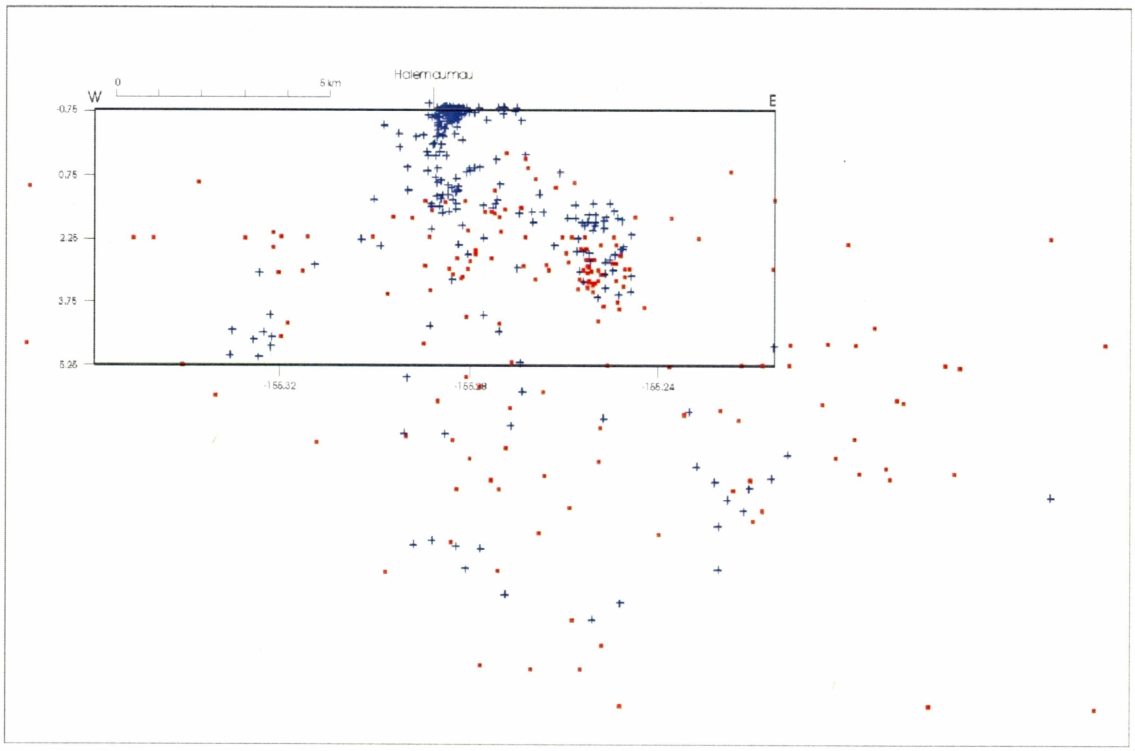

Figure11b: Comparison of HVO hypocenters from the same time period as the JUST 1996 experiment (red squares) with those from the final inversion (CDI) of this study (blue crosses). The inset shows the CDI study area. Side view, looking north.

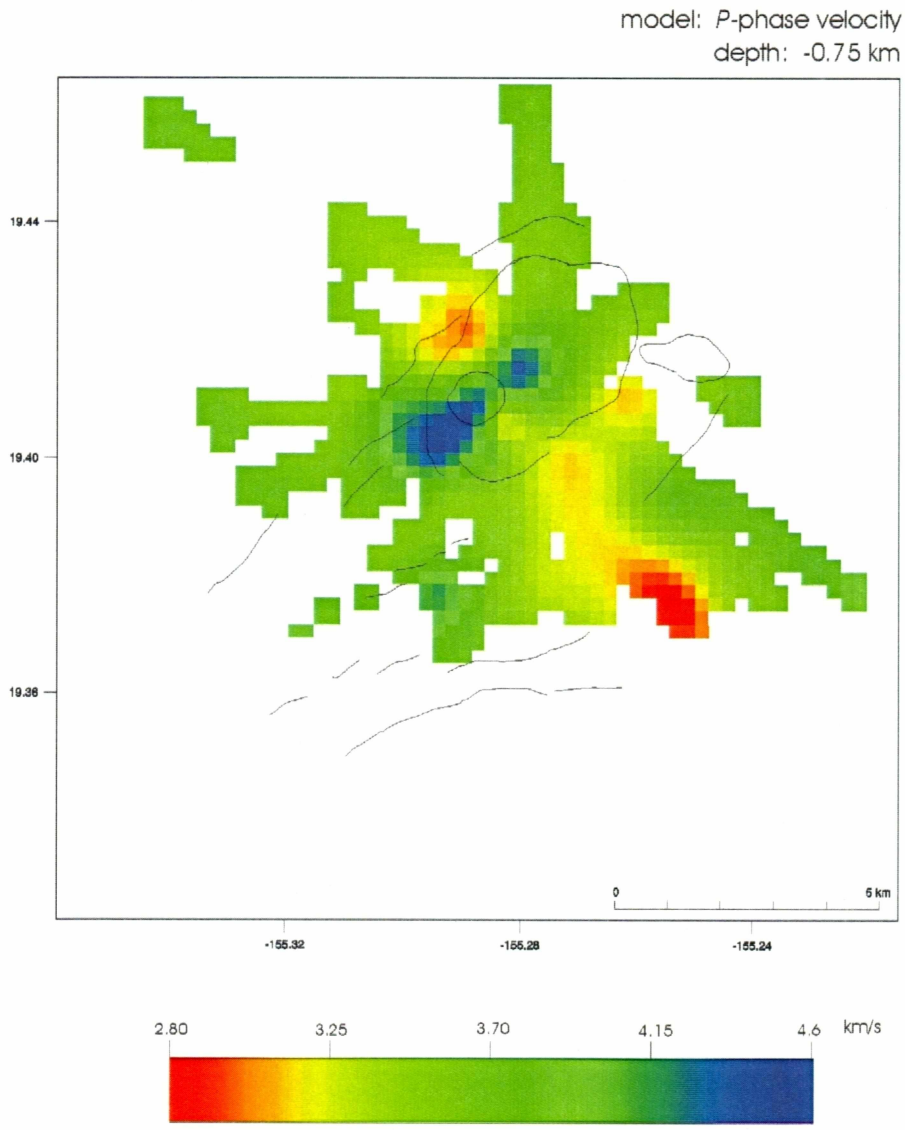

Figure 12a-k: CDI Vp model depth sections. Depth is indicated at the top of each figure and is relative to sea level, positive downward. The outline of Kilauea caldera, Halemaumau crater, and some of the faults are also shown.

Figure 12a.

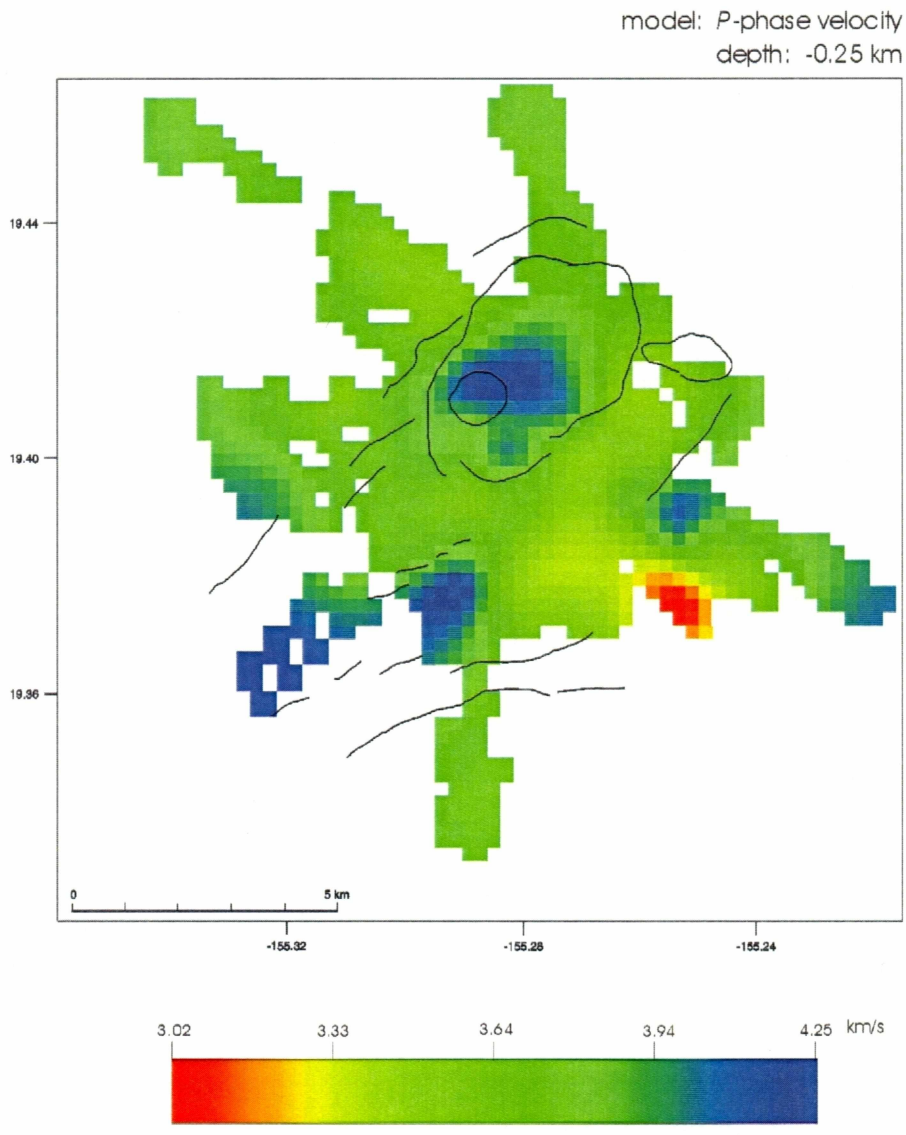
model: P-phase velocity
depth: -0.25 km
19.44
19.40
19.36
0
5 km
-155.32
-155.28
-155.24
3.02
3.33
3.64
3.94
4.25
km/s

Figure 12b.

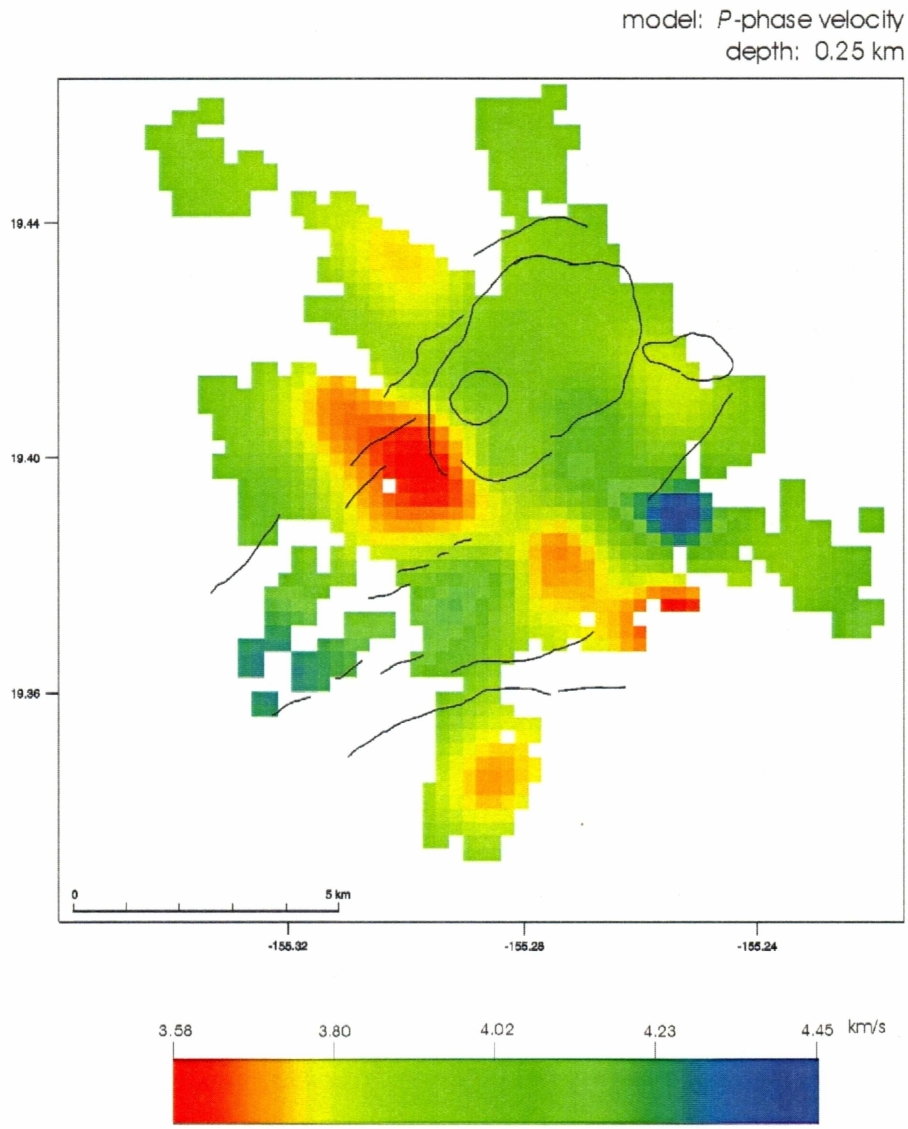
model: P-phase velocity
depth: 0.25 km
19.44
19.40
19.36
0
5 km
-155.32
-155.28
-155.24
3.58
3.80
4.02
4.23
4.45
km/s

Figure 12c.

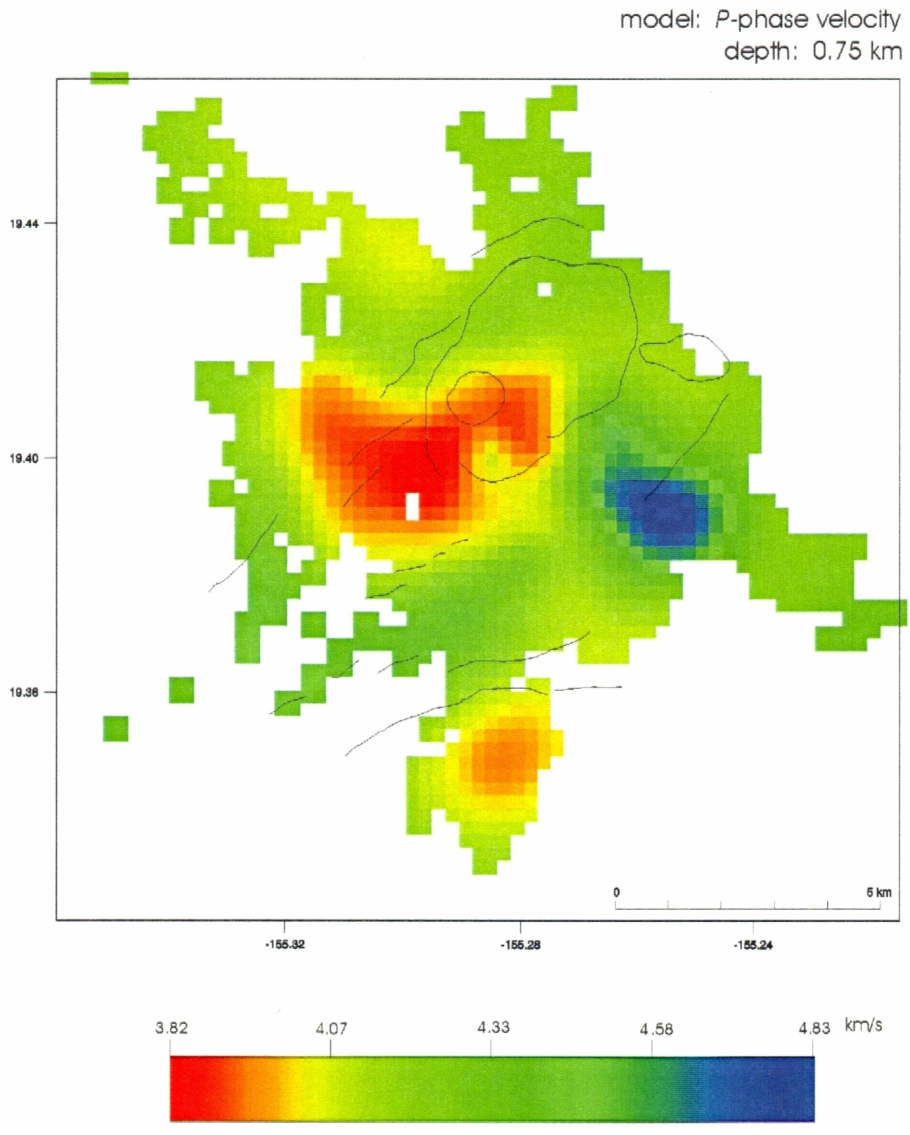
model: P-phase velocity
depth: 0.75 km
19.44
19.40
19.36
-155.32
-155.28
-155.24
0
5 km
3.82
4.07
4.33
4.58
4.83
km/s

Figure 12d.

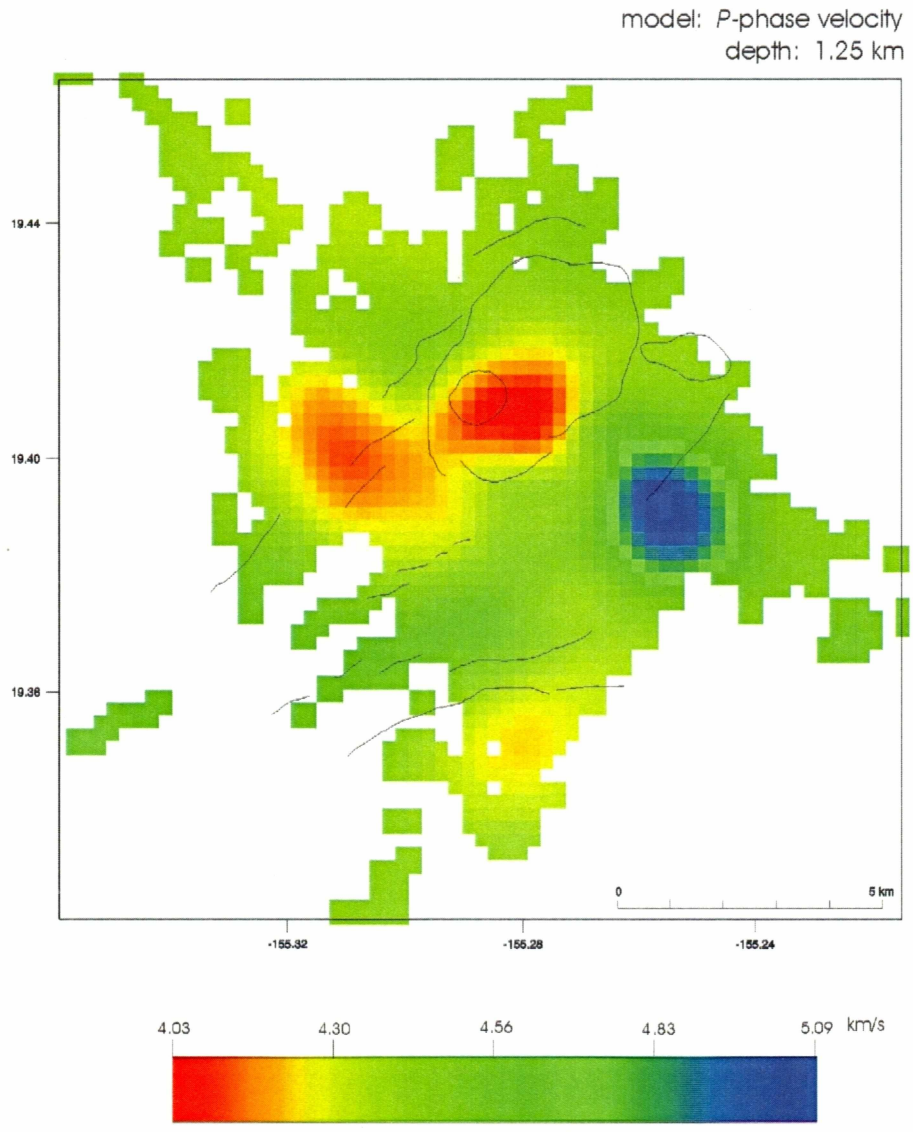
model: P-phase velocity
depth: 1.25 km
19.44
19.40
19.36
-155.32
-155.28
-155.24
0
5 km
4.03
4.30
4.56
4.83
5.09
km/s

Figure 12e.

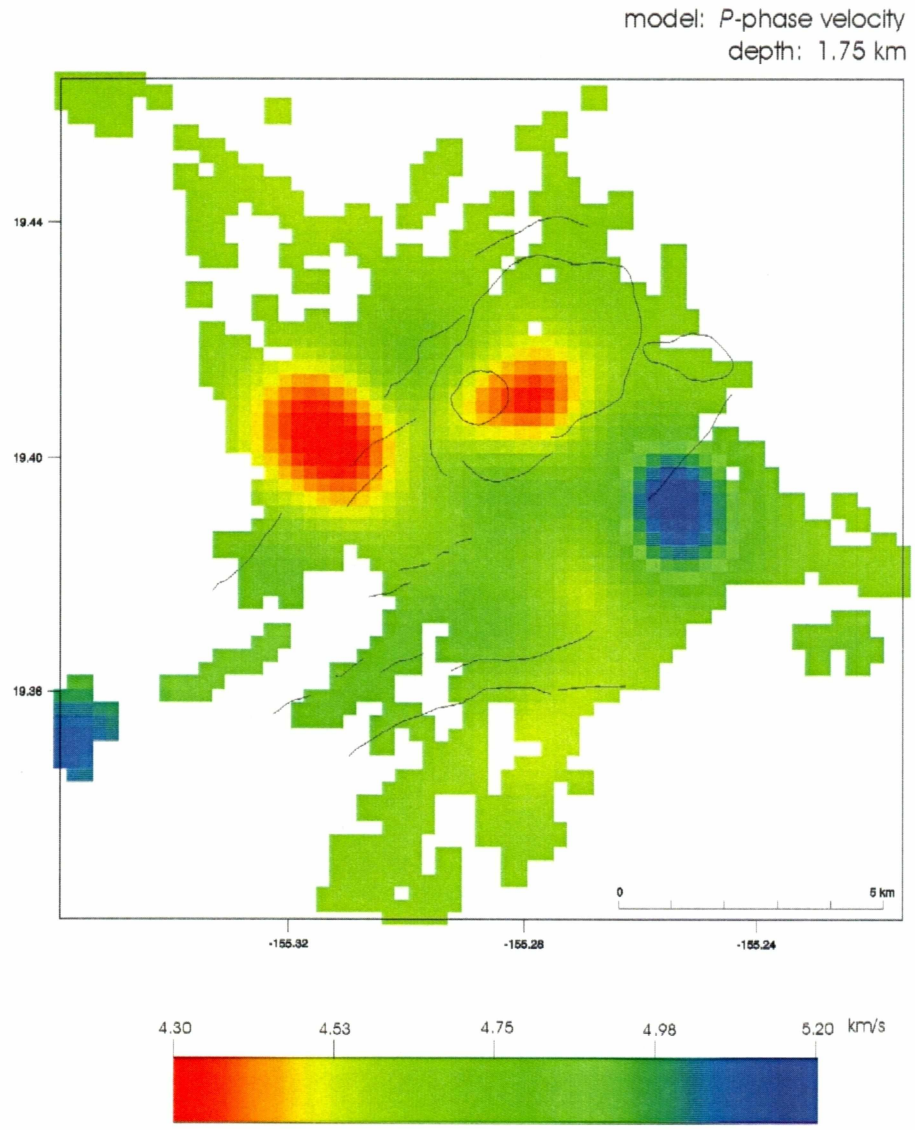
model: P-phase velocity
depth: 1.75 km
19.44
19.40
19.36
-155.32
-155.28
-155.24
0
5 km
4.30
4.53
4.75
4.98
5.20
km/s

Figure 12f.

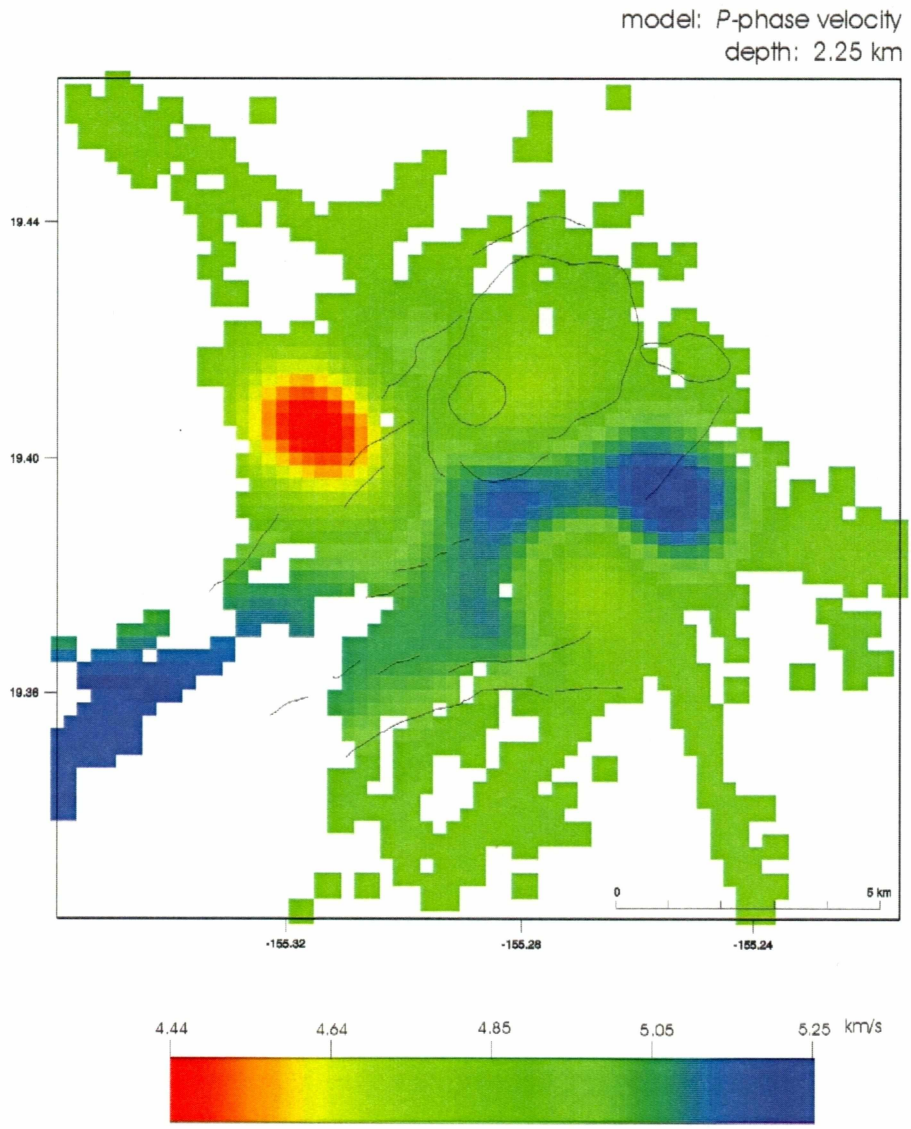
model: P-phase velocity
depth: 2.25 km
19.44
19.40
19.36
-155.32
-155.28
-155.24
0
5 km
4.44
4.64
4.85
5.05
5.25
km/s

Figure 12g.

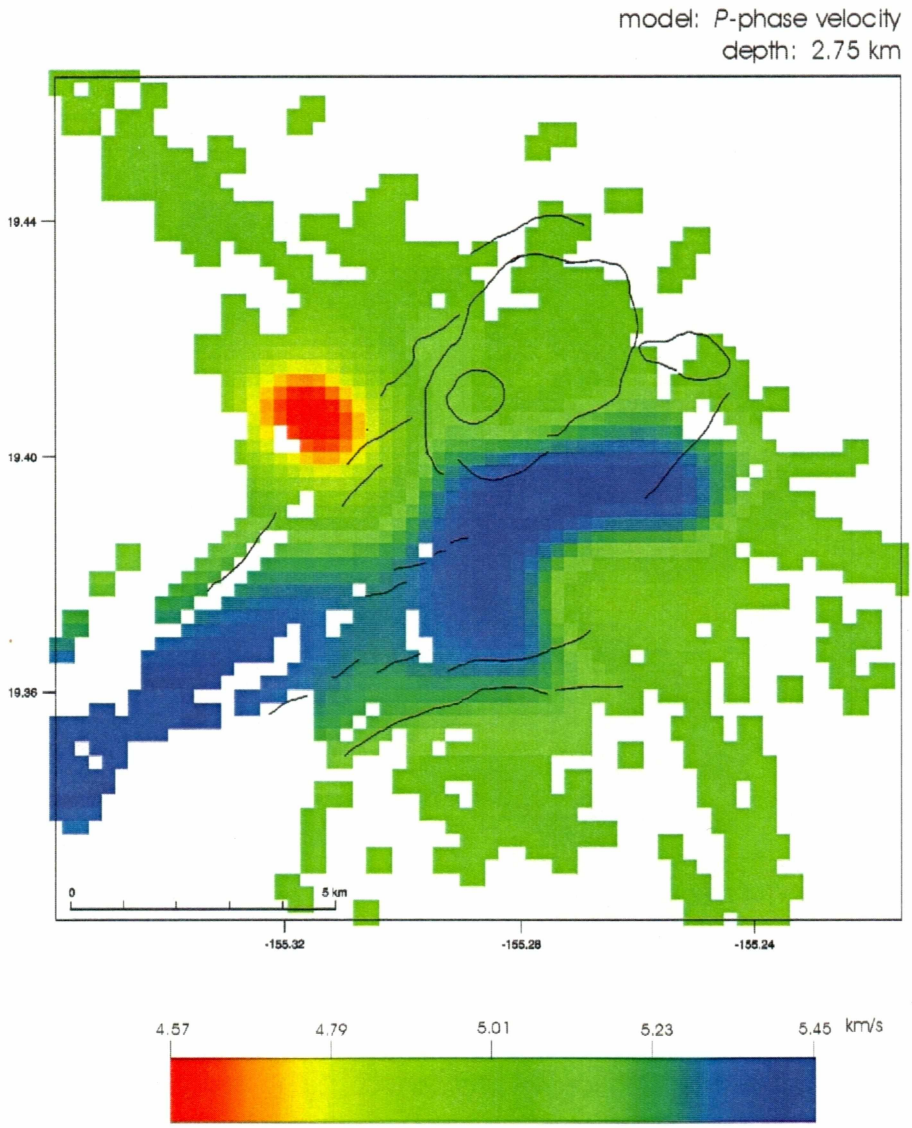
model: P-phase velocity
depth: 2.75 km
19.44
19.40
19.36
0
5 km
-155.32
-155.28
-155.24
4.57
4.79
5.01
5.23
5.45
km/s

Figure 12h.

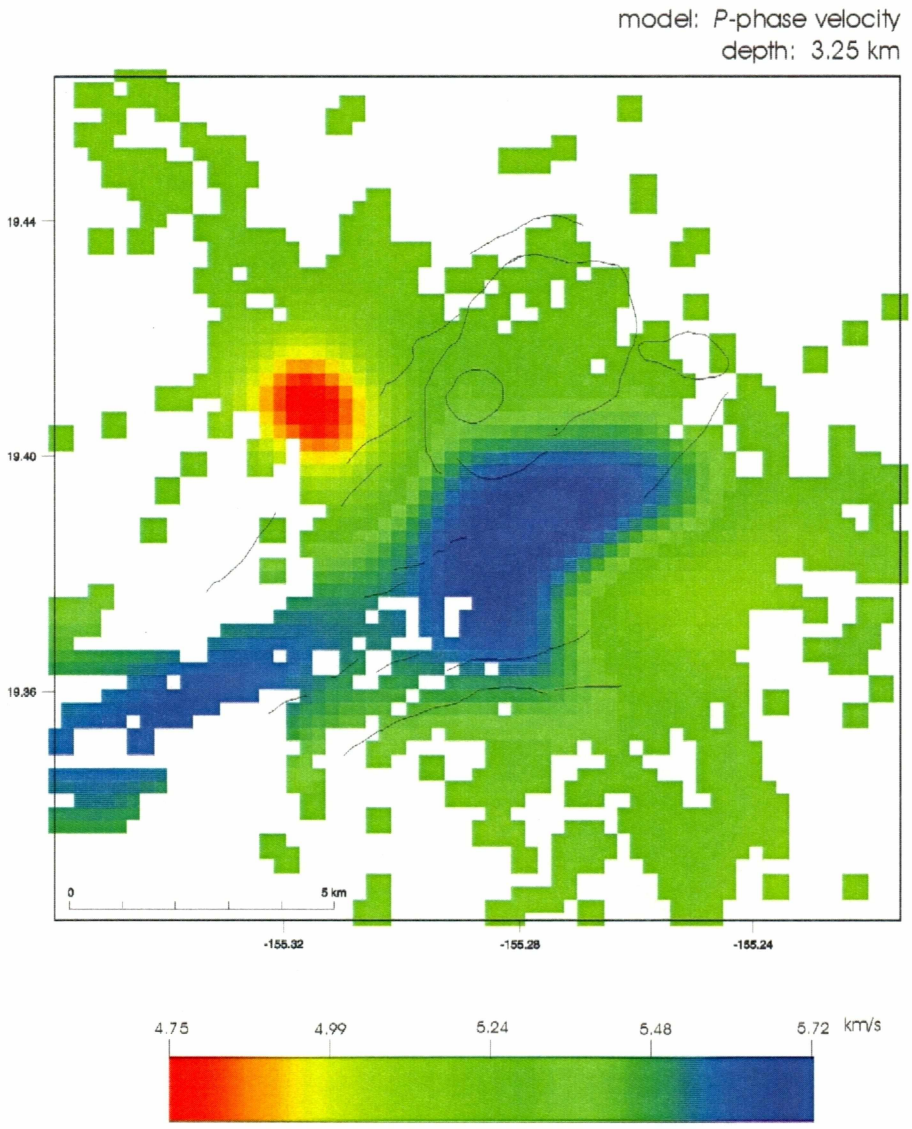
model: P-phase velocity
depth: 3.25 km
19.44
19.40
19.36
0
5 km
-155.32
-155.28
-155.24
4.75
4.99
5.24
5.48
5.72
km/s

Figure 12i.

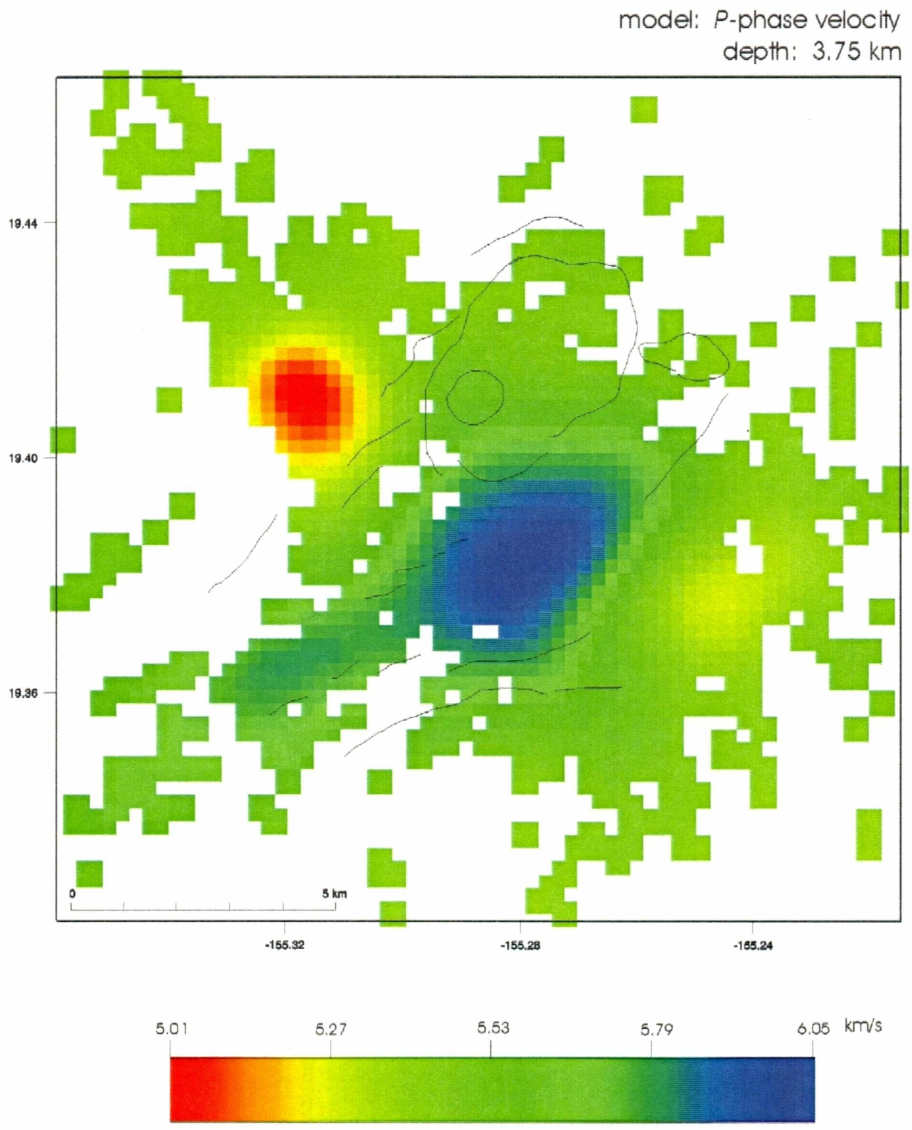
model: P-phase velocity
depth: 3.75 km
19.44
19.40
19.36
0
5 km
-155.32
-155.28
-155.24
5.01
5.27
5.53
5.79
6.05
km/s

Figure 12j.

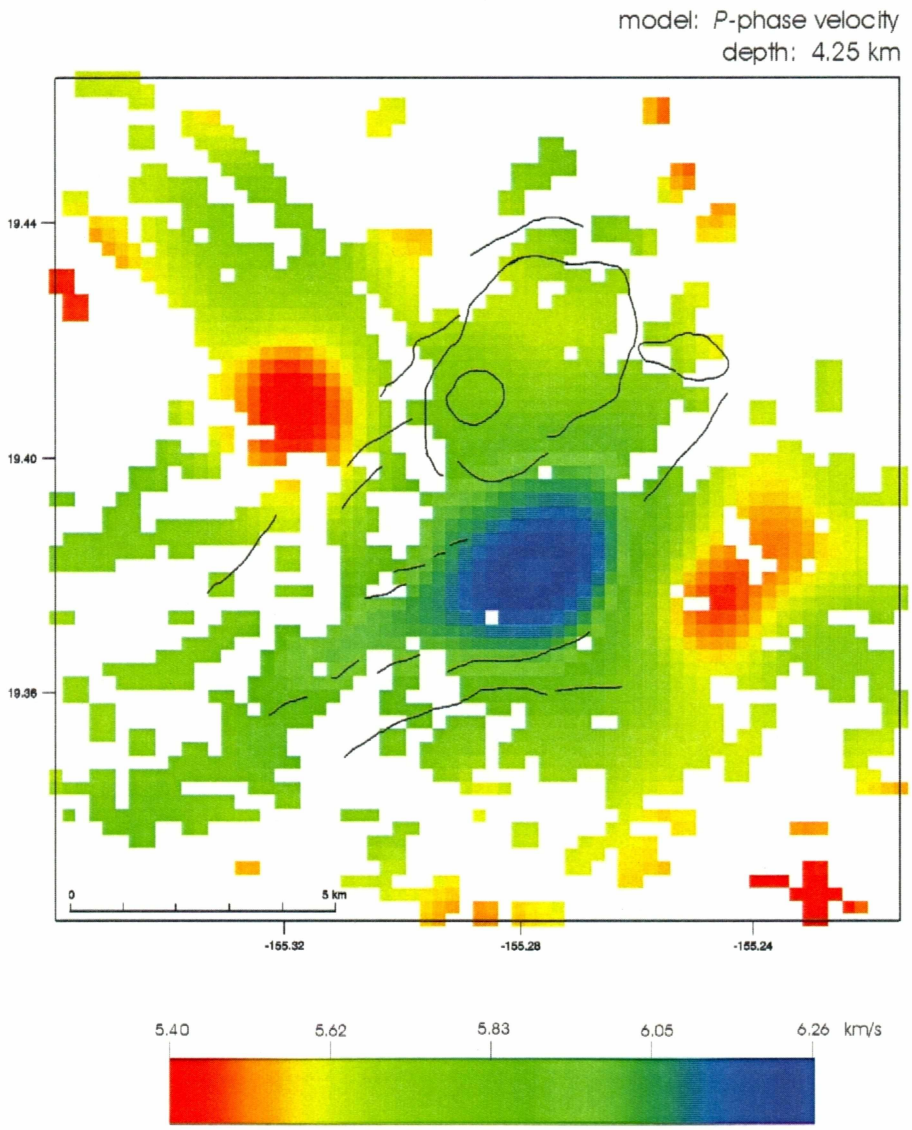
model: P-phase velocity
depth: 4.25 km
19.44
19.40
19.36
0
5 km
-155.32
-155.28
-155.24
5.40
5.62
5.83
6.05
6.26 km/s

Figure 12k.

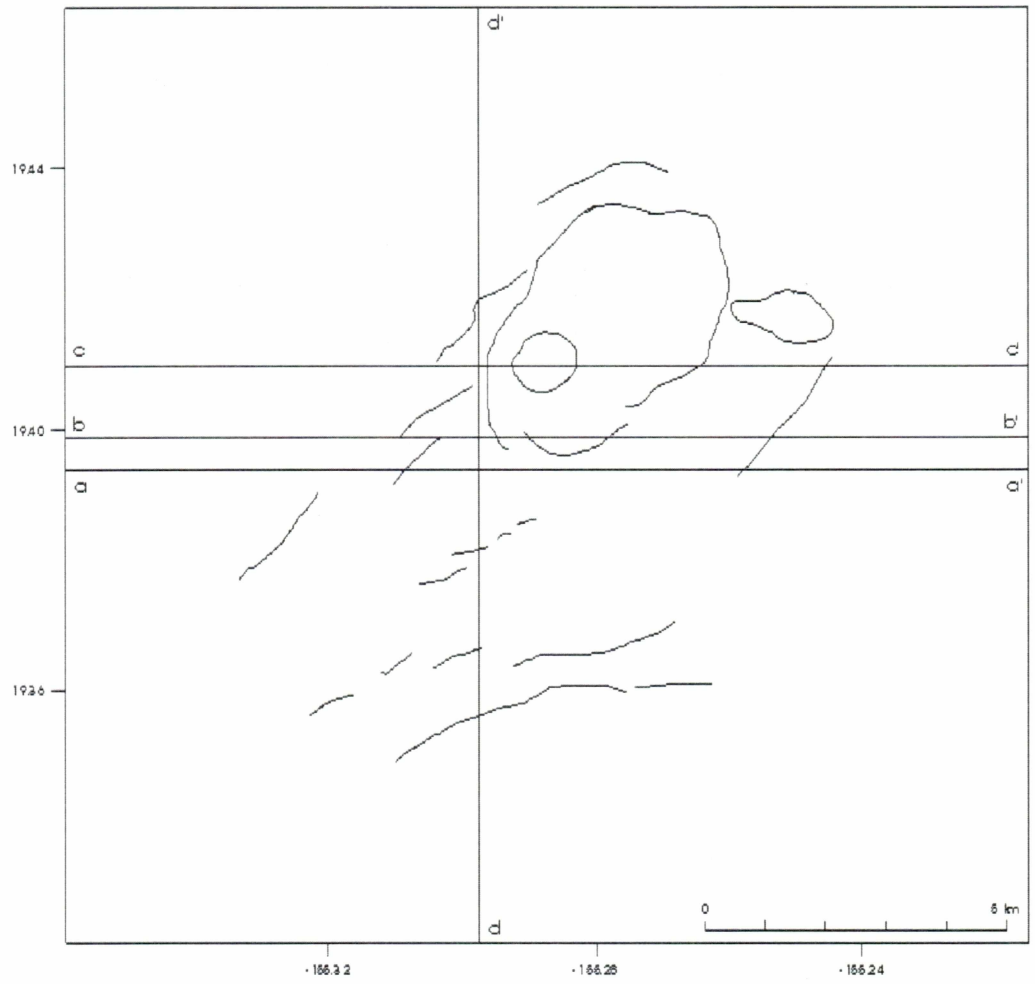

Figure 13: CDI Vp model cross-section locations for Figures 14a-d.

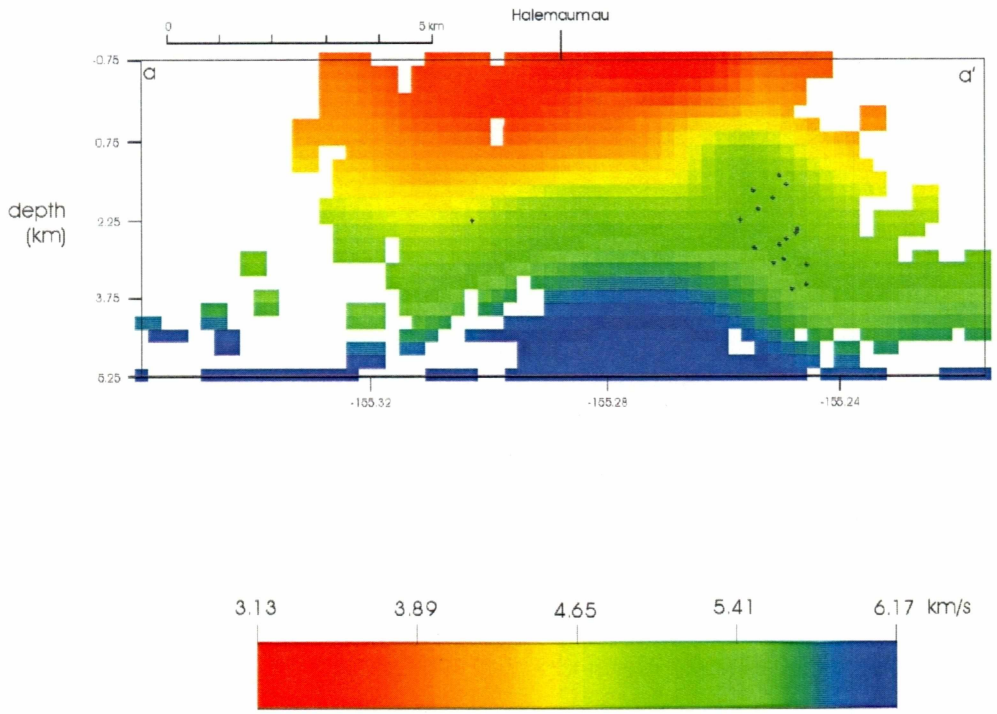

Figure 14a-d: CDI Vp model cross-sections.

Figure 14a: West to east section along line a-a' (see Figure 13 for location).

Hypocenters within 1km of the section are plotted as black dots.

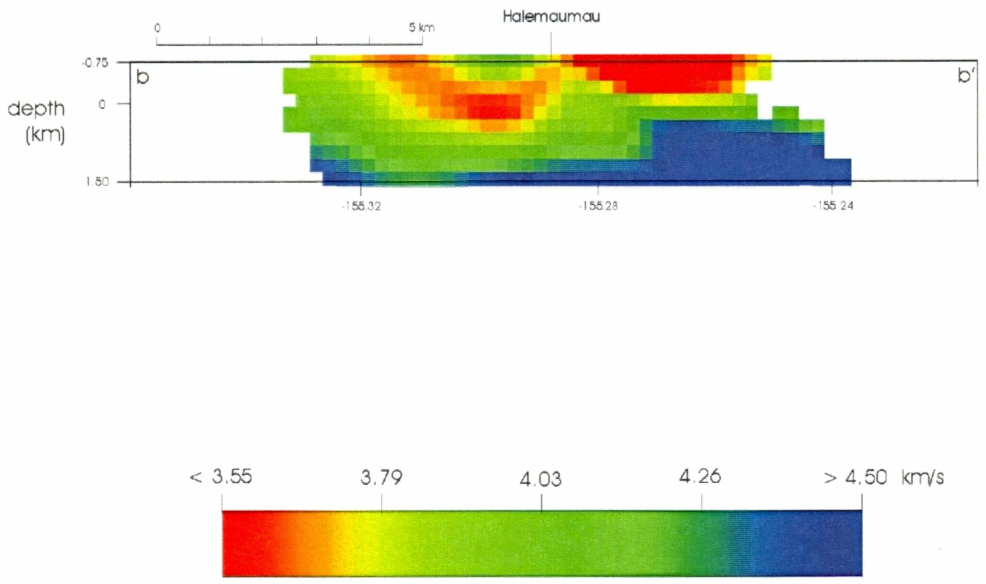

Figure 14b: West to east section along line b-b' (see Figure 13 for location). Section includes upper 10 layers (2.25 km) of the model, and the color scale has been tuned to highlight subtle features beneath Halemaumau.

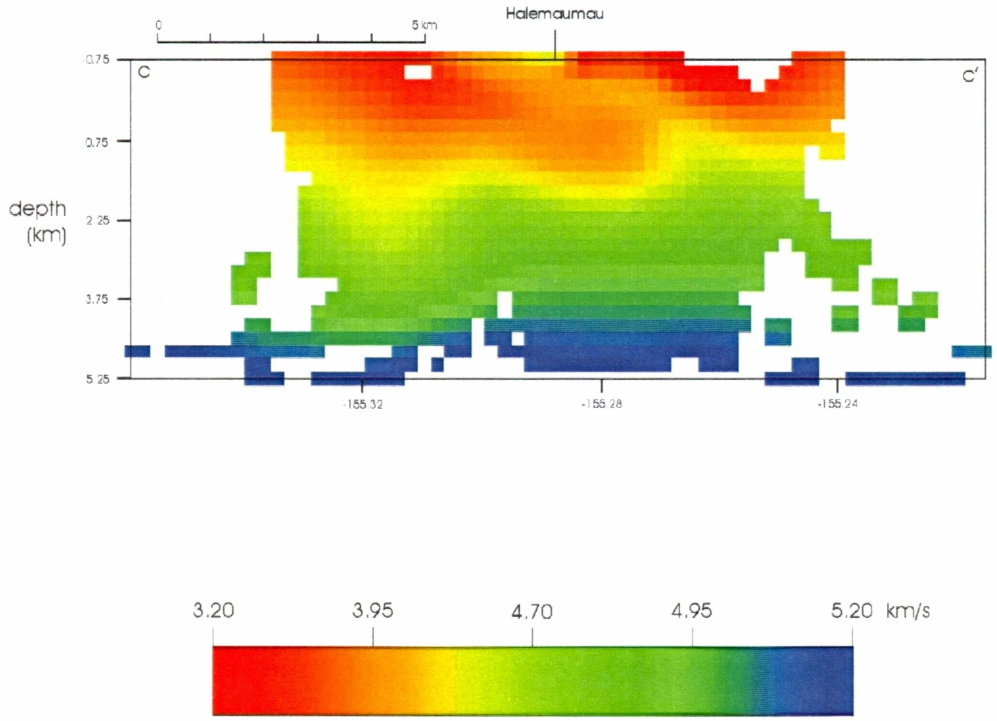

Figure 14c: West to east section along line c-c' (see Figure 13 for location).

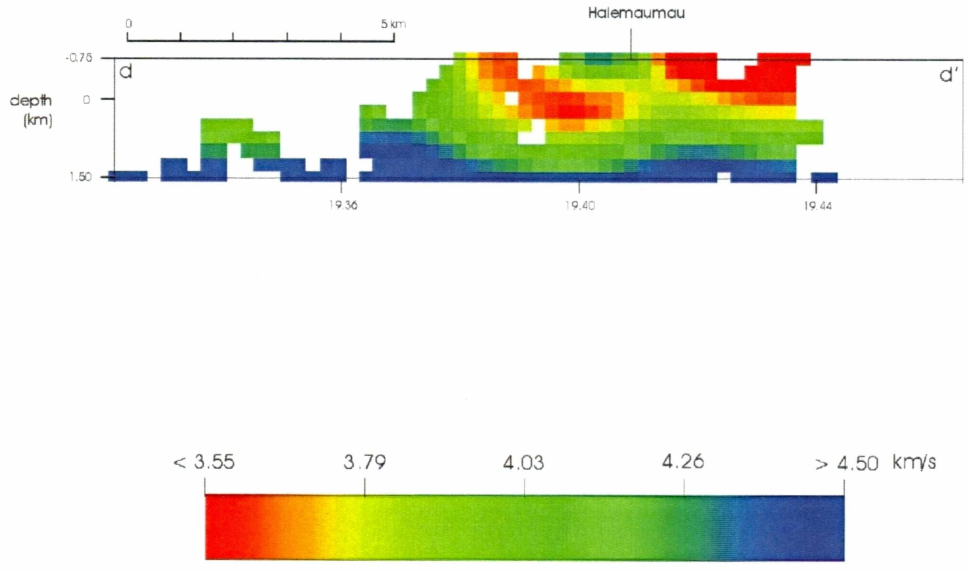

Figure 14d: South to north section along line d-d' (see Figure 13 for location). Section includes upper 10 layers (2.25 km) of the model, and the color scale has been tuned to highlight subtle features beneath Halemaumau.

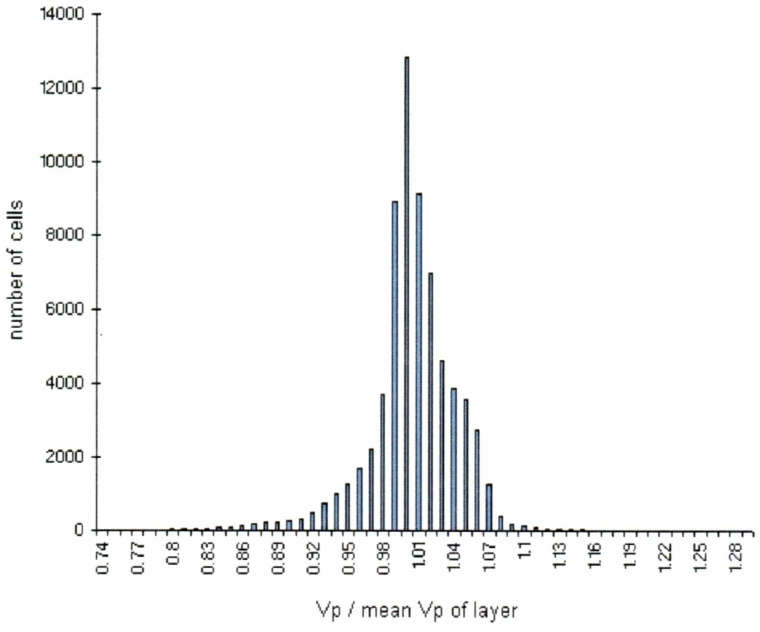

Figure 15: Histogram of normalized P-phase velocities from the CDI model. The Vp in each cell is normalized by the mean Vp of the layer. Values greater than one represent high-Vp and values below 1 represent low-Vp. The volume of the cells with a proportional Vp less than or equal to 0.91 is 26.2 ^{km3}.

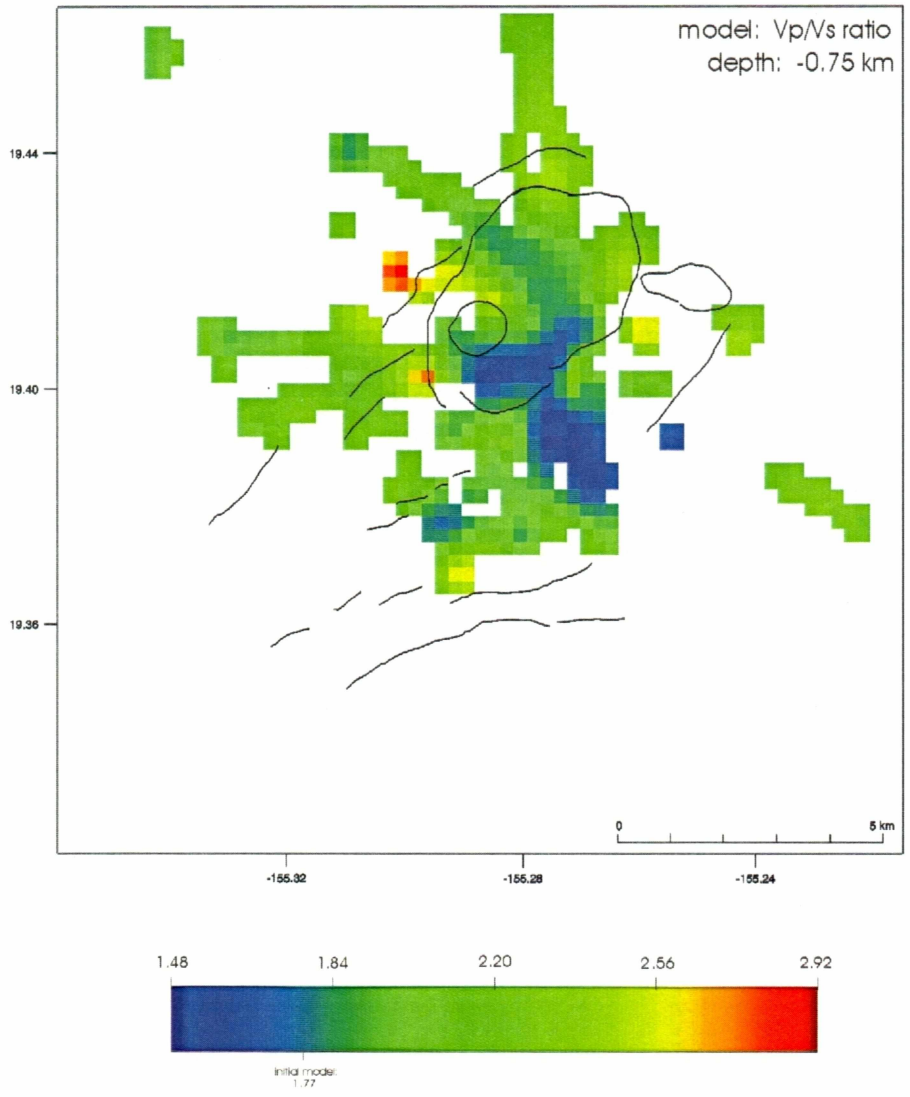

Figure 16a-l: CDI Vp/Vs model depth sections. Depth is indicated at the top of each figure and is relative to sea level, positive downward. The outline of Kilauea caldera, Halemaumau crater, and some of the faults are also shown.

Figure 16a.

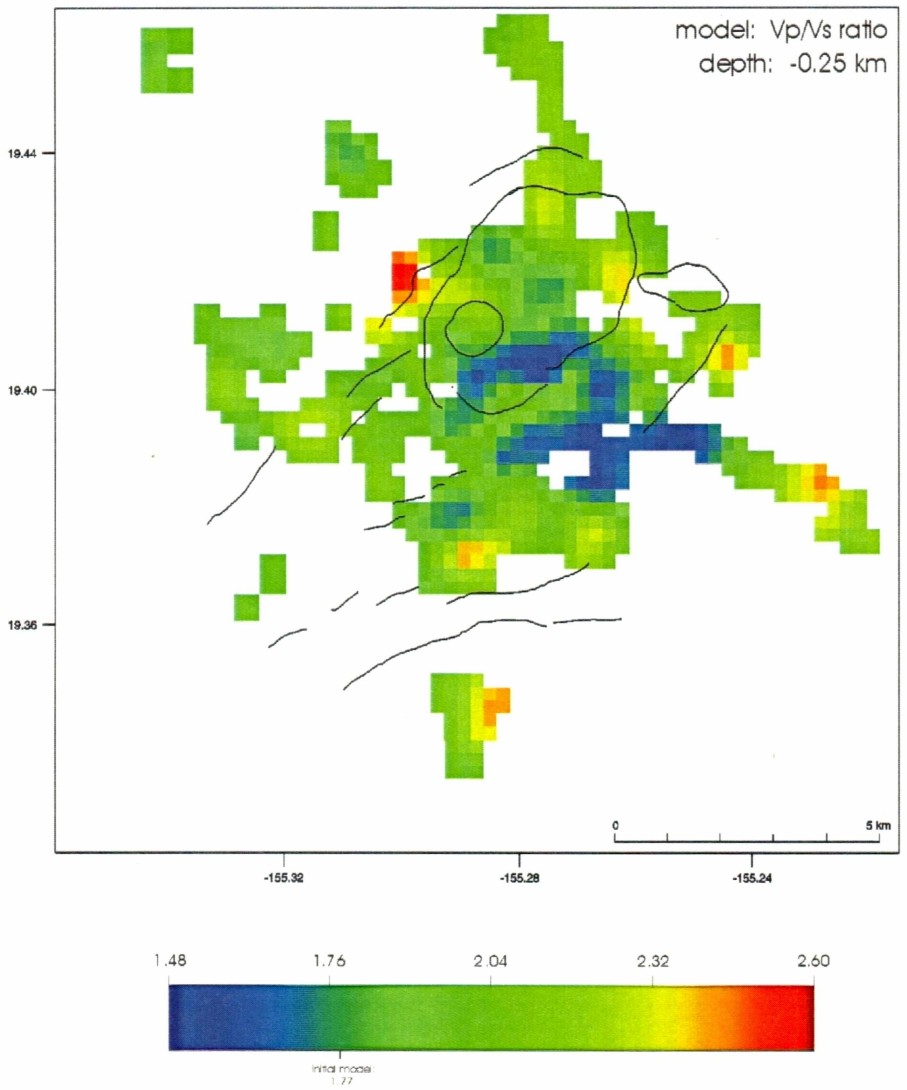
model: Vp/Vs ratio
depth: -0.25 km
19.44
19.40
19.36
-155.32
-155.28
-155.24
0
5 km
1.48
1.76
2.04
2.32
2.60
initial model
1.77

Figure 16b.

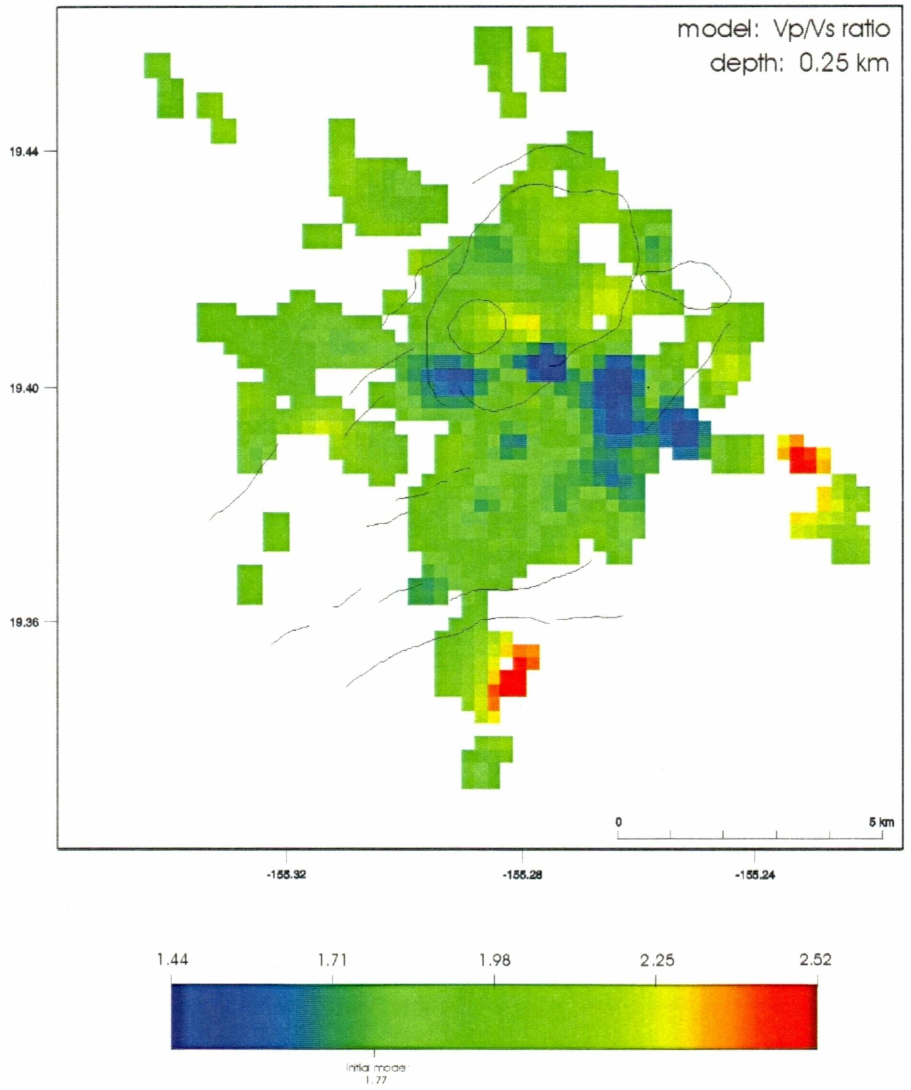
model: Vp/Vs ratio
depth: 0.25 km
19.44
19.40
19.36
0
5 km
-155.32
-155.28
-155.24
1.44
1.71
1.98
2.25
2.52
Initial model
1.77

Figure 16c.

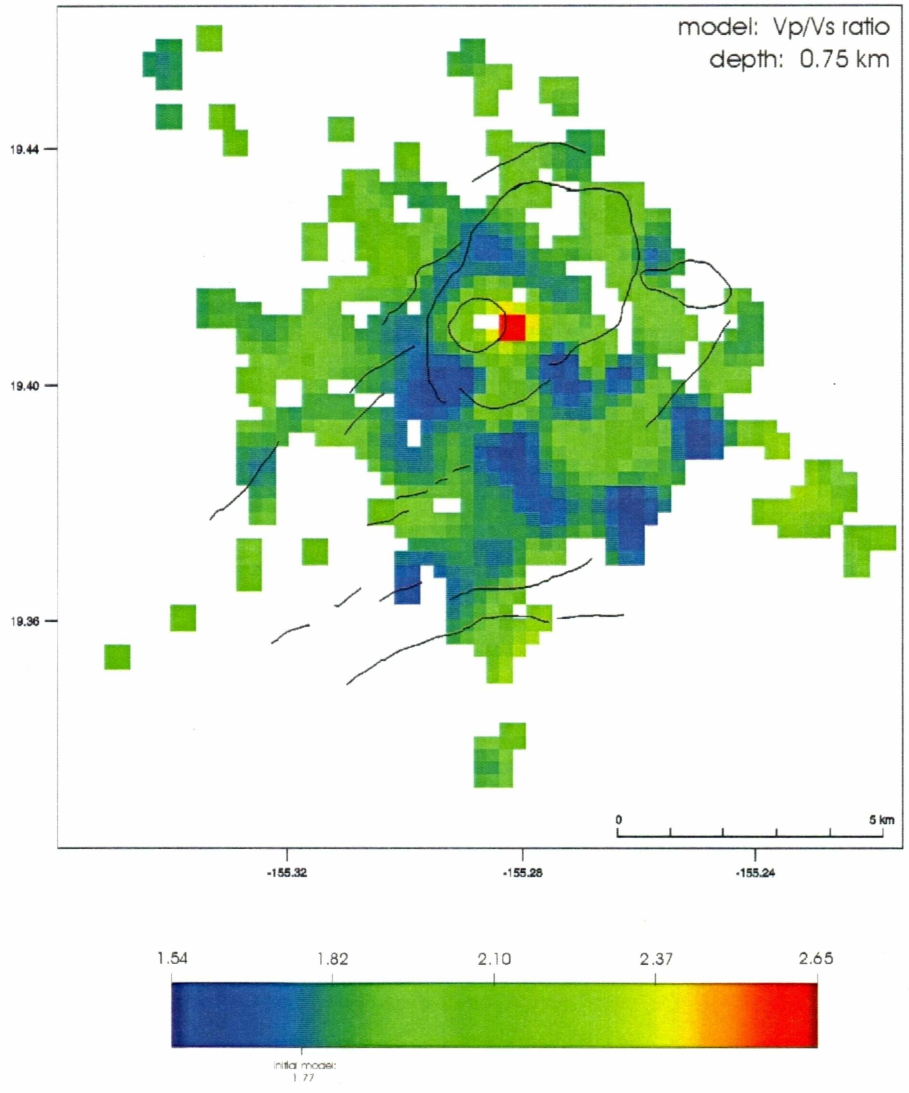
model: Vp/Vs ratio
depth: 0.75 km
19.44
19.40
19.36
-155.32
-155.28
-155.24
0
5 km
1.54
1.82
2.10
2.37
2.65
initial model:
1.77

Figure 16d.

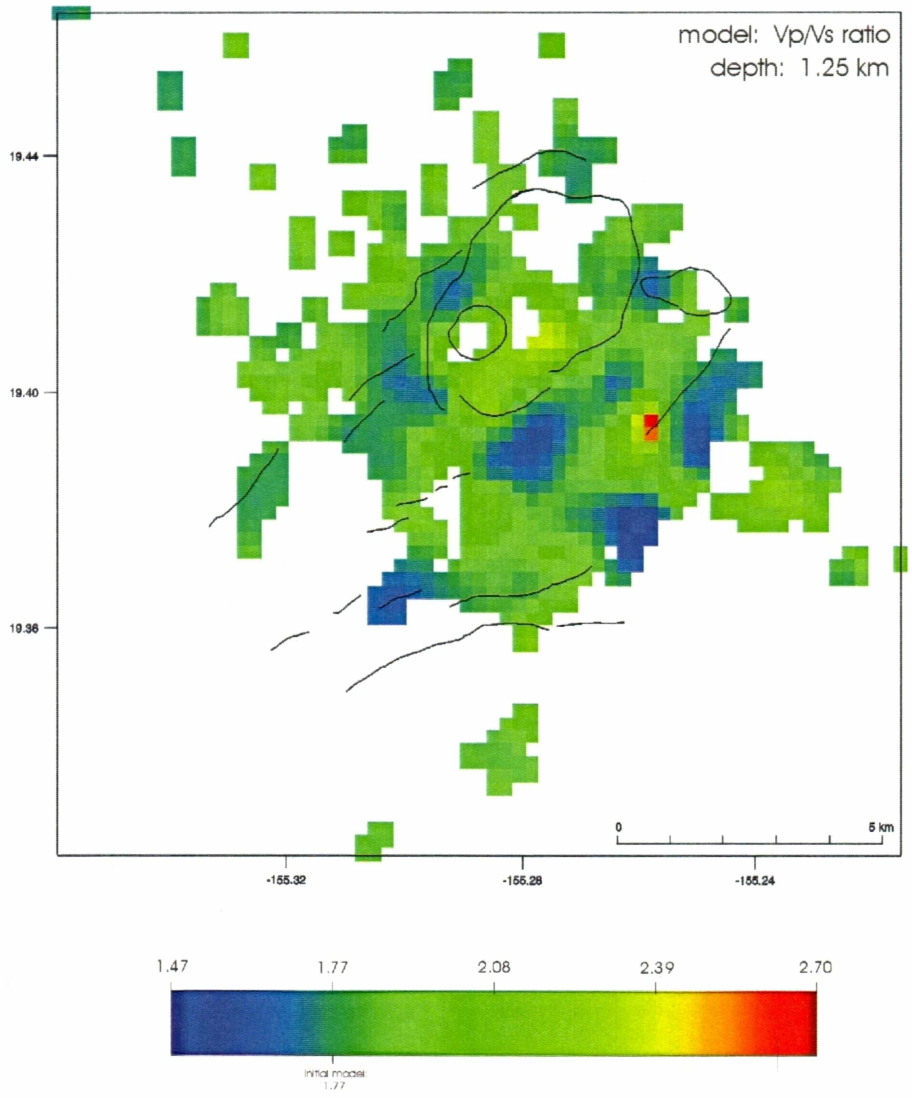
model: Vp/Vs ratio
depth: 1.25 km
19.44
19.40
19.36
-155.32
-155.28
-155.24
0
5 km
1.47
1.77
2.08
2.39
2.70
initial model
1.77

Figure 16e.

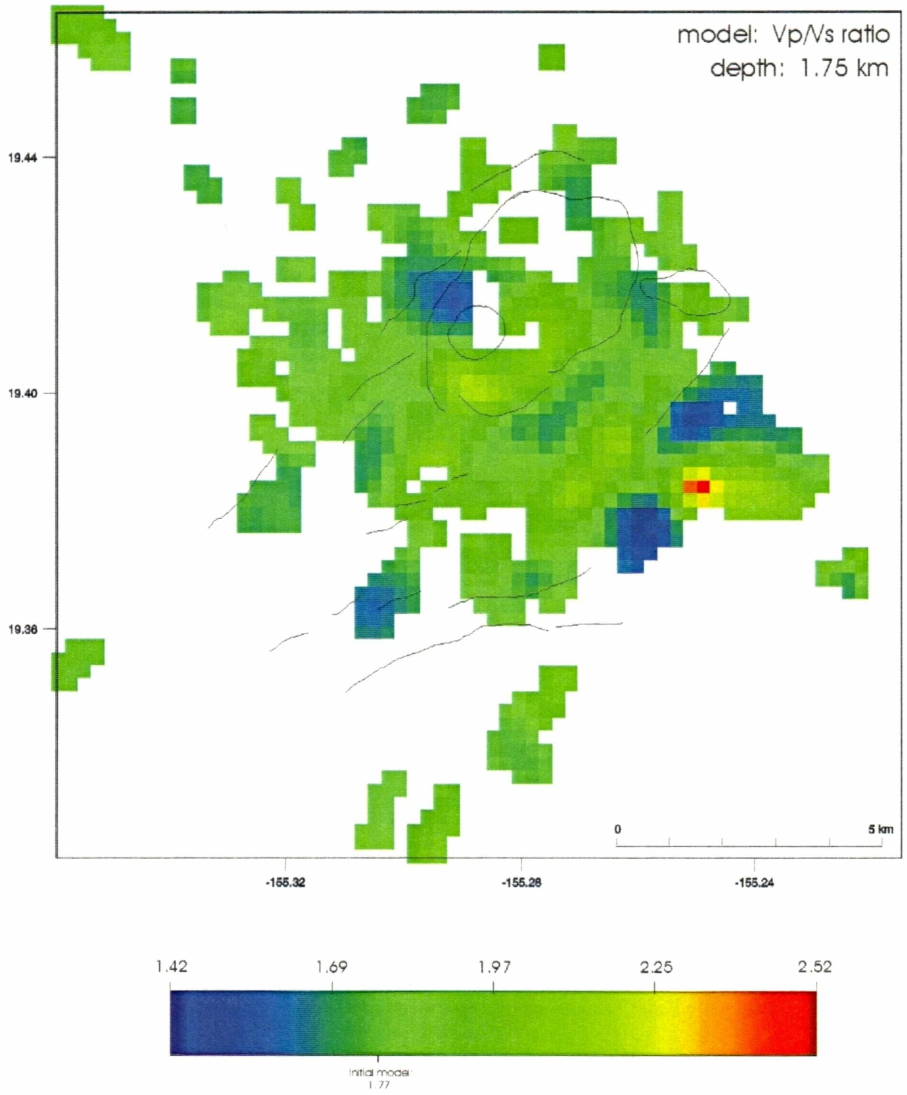
model: Vp/Vs ratio
depth: 1.75 km
19.44
19.40
19.36
-155.32
-155.28
-155.24
0
5 km
1.42
1.69
1.97
2.25
2.52
Initial model
1.77

Figure 16f.

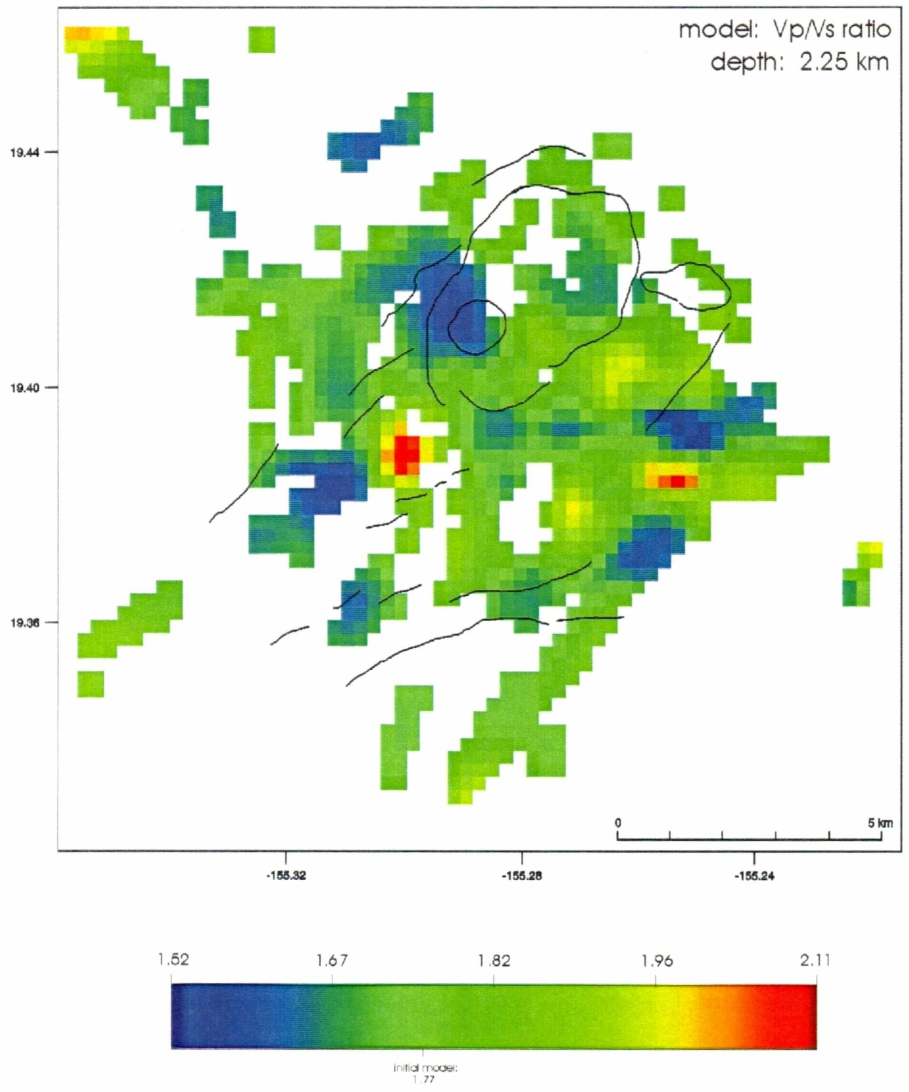

Figure 16g.

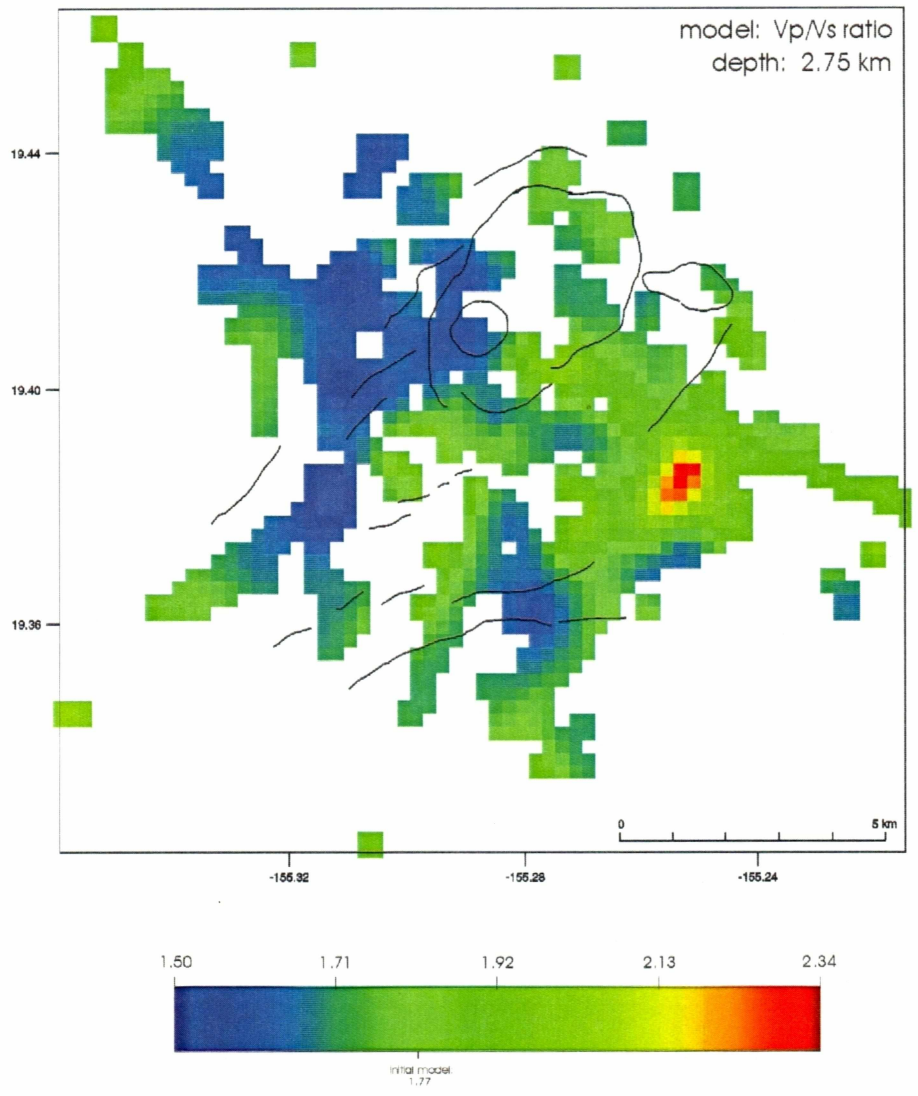
model: Vp/Vs ratio
depth: 2.75 km
19.44
19.40
19.36
-155.32
-155.28
-155.24
0
5 km
1.50
1.71
1.92
2.13
2.34
initial model
1.77

Figure 16h.

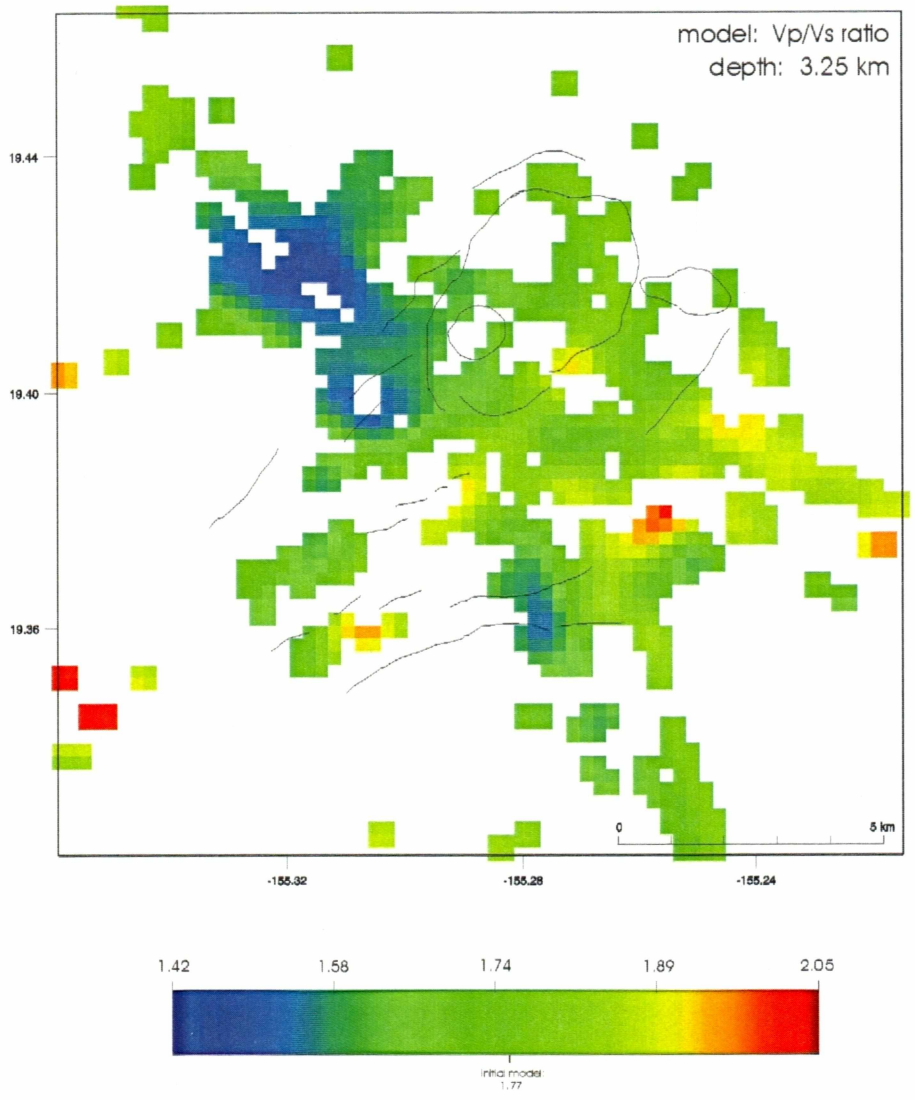
model: Vp/Vs ratio
depth: 3.25 km
19.44
19.40
19.36
-155.32
-155.28
-155.24
0
5 km
1.42
1.58
1.74
1.89
2.05
initial model
1.77

Figure 16i.

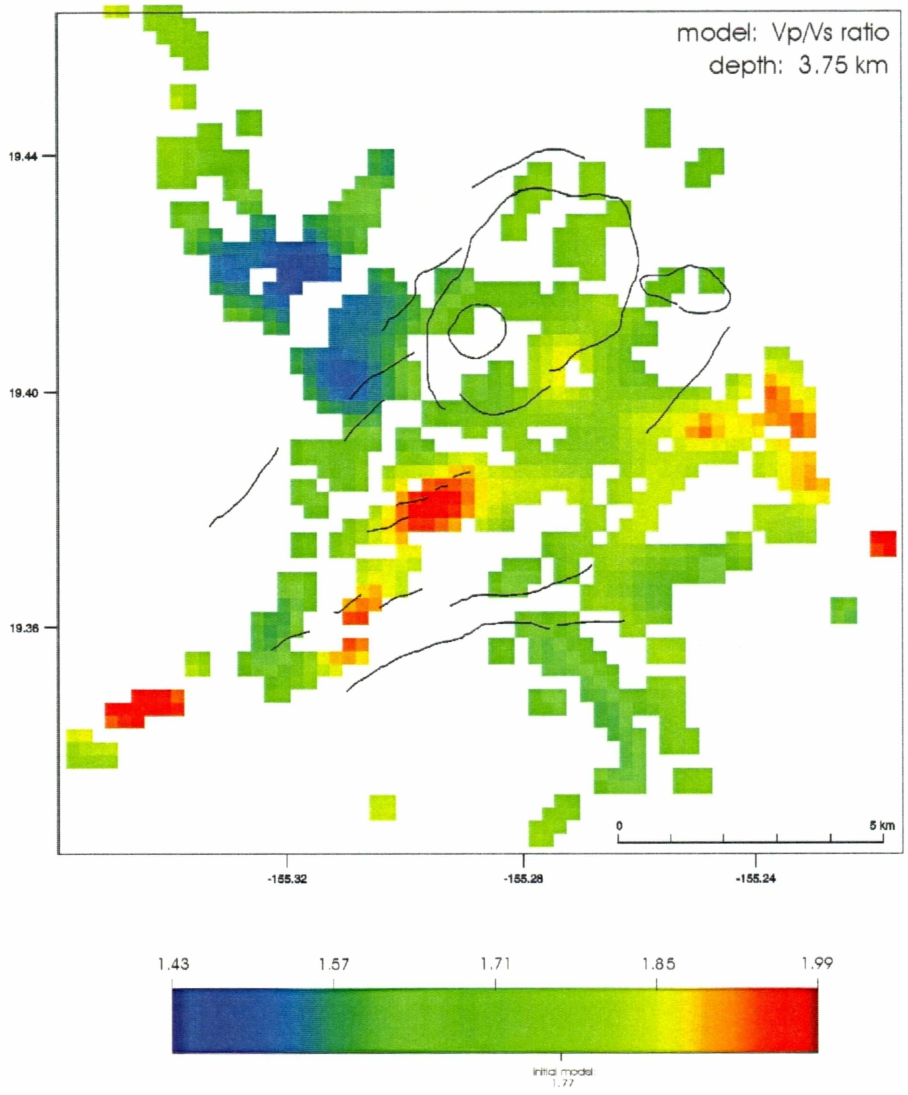
model: Vp/Vs ratio
depth: 3.75 km
19.44
19.40
19.36
0
5 km
-155.32
-155.28
-155.24
1.43
1.57
1.71
1.85
1.99
initial model
1.77

Figure 16j.

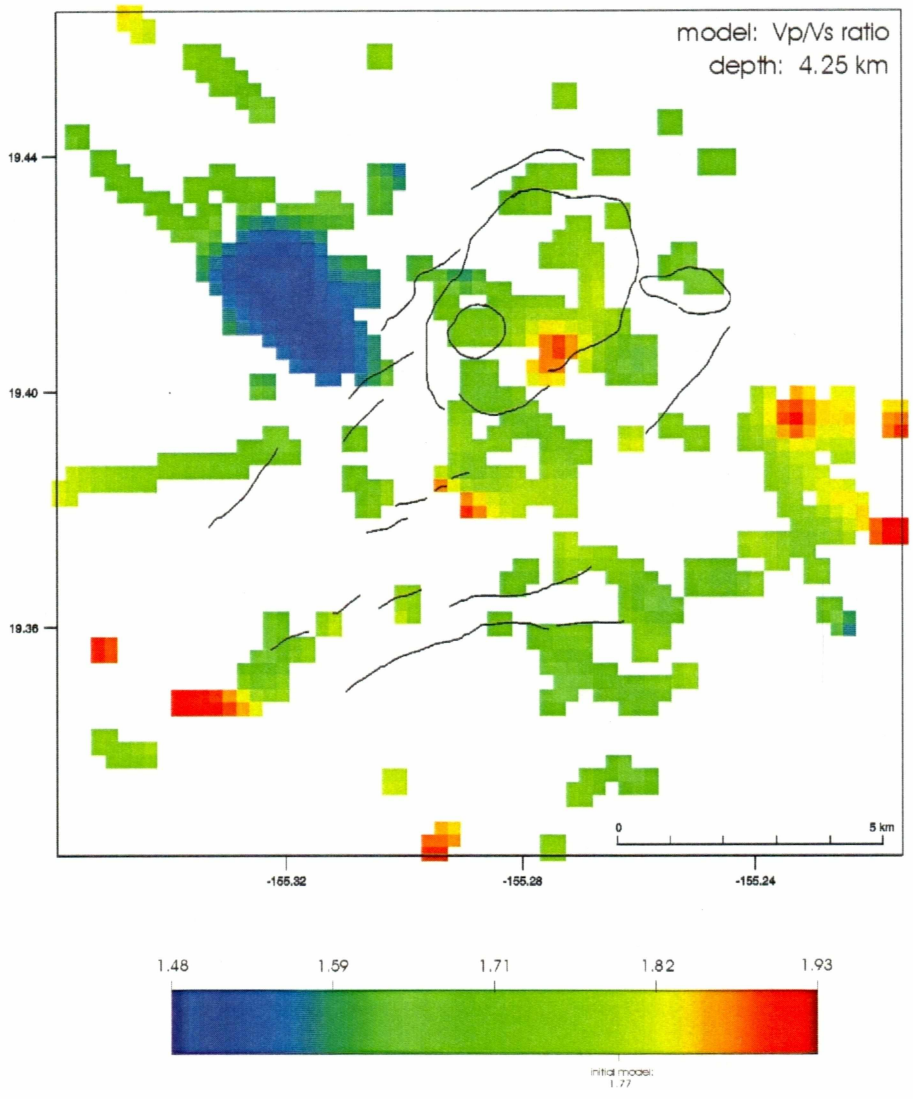
model: Vp/Vs ratio
depth: 4.25 km
19.44
19.40
19.36
-155.32
-155.28
-155.24
0
5 km
1.48
1.59
1.71
1.82
1.93
initial model:
1.77

Figure 16k.

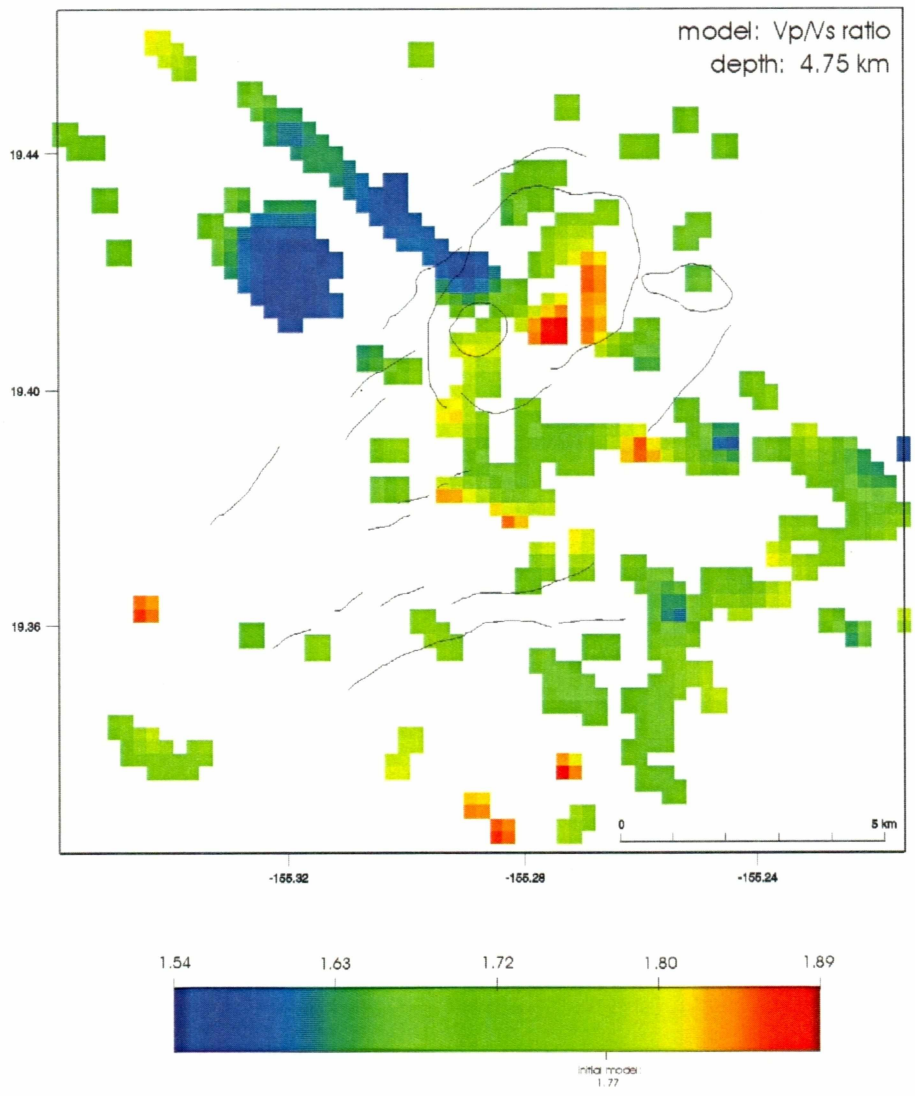
model: Vp/Vs ratio
depth: 4.75 km
19.44
19.40
19.36
-155.32
-155.28
-155.24
0
5 km
1.54
1.63
1.72
1.80
1.89
initial model
1.77

Figure 16l.

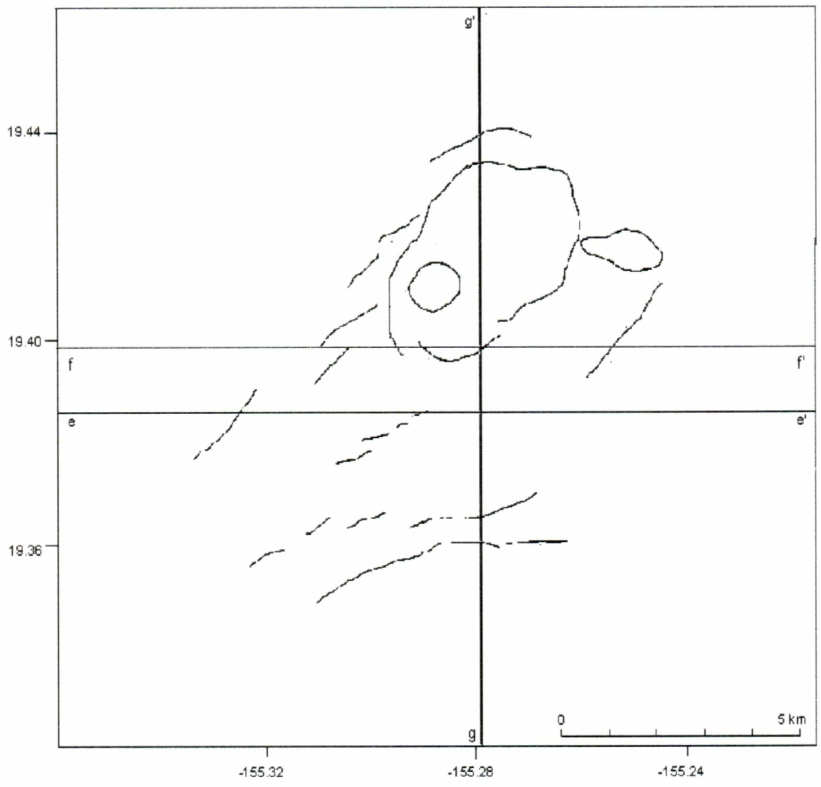

Figure 17: CDI Vp/Vs model cross-section locations for Figures 18a-c.

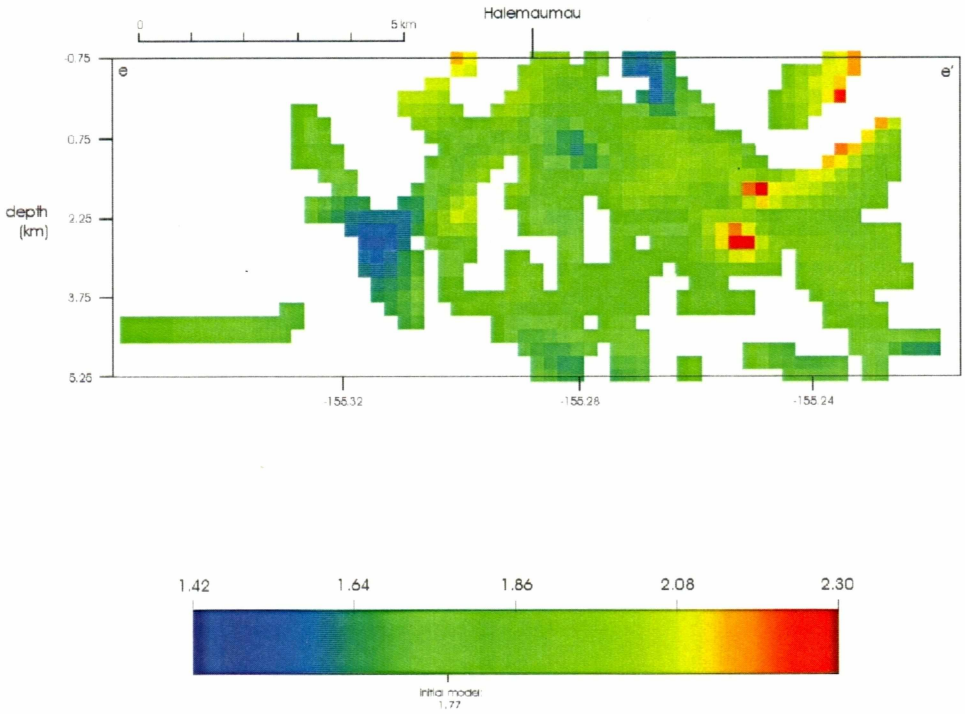

Figure 18a-c: CDI Vp model cross-sections.

Figure 18a: West to east section along line e-e' (see Figure 17 for location).

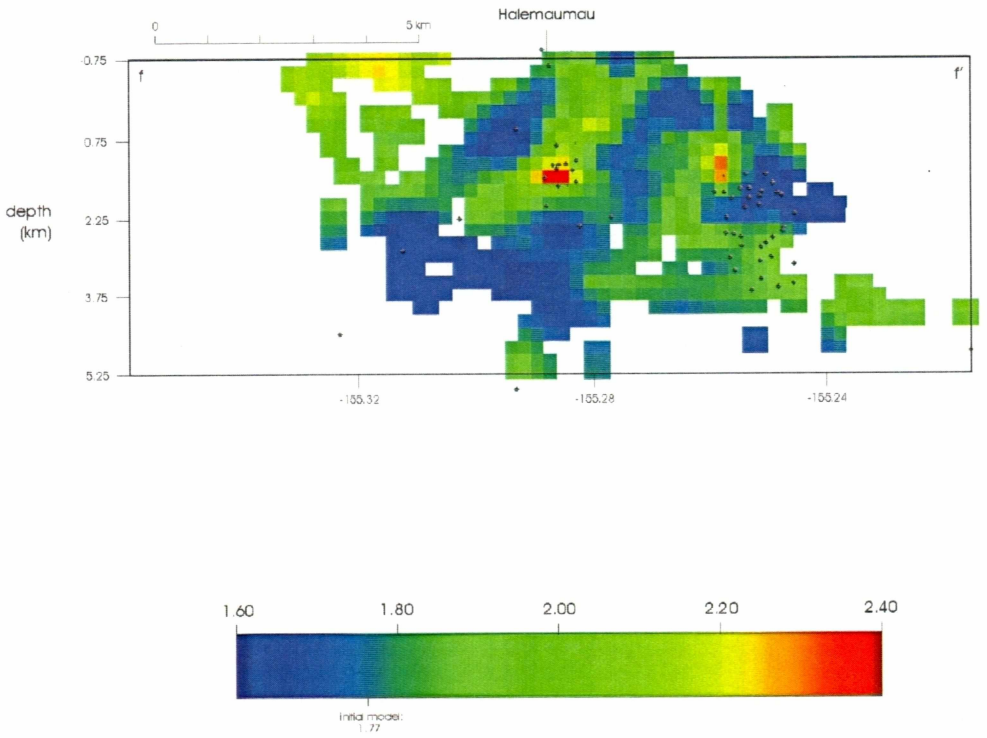

Figure 18b: West to east section along line f-f' (see Figure 17 for location).

Hypocenters within 1km of the section are plotted as black dots.

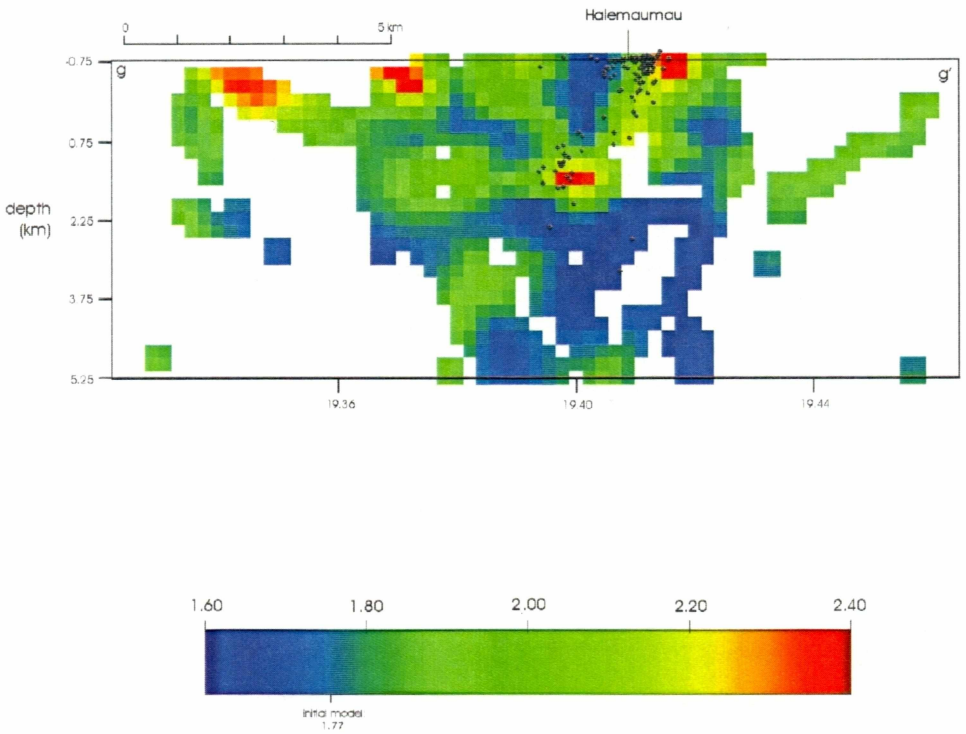

Figure 18c: South to north section along line g-g' (see Figure 17 for location). Hypocenters within 1km of the section are plotted as black dots.